QA:L

FULL SCALE TOMOGRAPHIC SEISMIC IMAGING OF THE POTENTIAL REPOSITORY HORIZON MILESTONE REPORT SP3B2FM4

Document I.D.#BA0000000-01717-5700-00019

P.I.: Ernest L. Majer
R. Gritto
T.M. Daley
V.A. Korneev
M.A. Feighner
J.E. Peterson

NOT APPROVED

DO NOT COPY OR DUPLICATE

September 30, 1998

Earth Sciences Division
E.O. Lawrence Berkeley National Laboratory

Revision 00C

9903020093 990223
PDR WASTE
WM-11 PDR

ACKNOWLEDGEMENTS

Technical review of this work was conducted by the following technical staff of E.O. Lawrence Berkeley National Laboratory: L. Johnson and D. Vasco. The careful review and responsiveness of the reviewers is most appreciated. EA review was conducted by N. Aden-Gleason. The authors would also like to thank S. Link for coordinating the submittal and retrieval of data from the Technical Database (TDB). Finally, the authors thank C. Taliaferro and Maryann Villavert for producing the document. This work was supported by the Director, Office of Civilian Radioactive Waste Management, through a Memorandum Purchase Order EA9013MC5X between TRW Environmental Safety Systems, Inc. and the Ernest Orlando Lawrence Berkeley National Laboratory of the Yucca Mountain Site Characterization Project through U.S. Department of Energy Contract No. DE-AC03-76SF00098.

DO NOT COPY OR DUPLICATE

NOT APPROVED

TABLE OF CONTENTS

Abstract 1
1. Introduction 1
2. Quality Assurance Status 2
3. Purpose of the Test 3
4. Description of Potential Tests 4
5. Selection of Prototype Tests 5
6. Prototype Field Experiments and Modeling 6
7. Final Survey Design and Execution 9
8. Data Processing: 10
8.1. Sorting and Filtering 10
8.2. 2D-3D Modeling Theory 11
8.3. Zero Offset Analysis: 11
8.4. Ray Tracing: 12
8.5. Tomographic Imaging: 13
8.6. Static Corrections 14
9. Reprocessing of Surface Seismic YMP-3 16
10. Results and Conclusions: 17
11. Future Work 20
References: 22

NOT APPROVED

DO NOT COPY OR DUPLICATE

TABLE OF CONTENTS

Abstract 1
1. Introduction 1
2. Quality Assurance Status 2
3. Purpose of the Test 3
4. Description of Potential Tests 4
5. Selection of Prototype Tests 5
6. Prototype Field Experiments and Modeling 6
7. Final Survey Design and Execution 9
8. Data Processing: 10
8.1. Sorting and Filtering 10
8.2. 2D-3D Modeling Theory 11
8.3. Zero Offset Analysis: 11
8.4. Ray Tracing: 12
8.5. Tomographic Imaging: 13
8.6. Static Corrections 14
9. Reprocessing of Surface Seismic YMP-5 16
10. Results and Conclusions: 17
11. Future Work 20
References: 22

NOT APPROVED

DO NOT COPY OR DUPLICATE

ABSTRACT

A comprehensive program to use tomographic methods to map the potential repository volume was initiated in December of 1997. The approach was staged into different phases. An initial phase used P- and S-wave vibrators on-line YMP-5 and YMP-6 for seismic sources and 3-component geophones in the ESF at 39+00 m to determine feasibility of tomography and a second phase in which a full scale experiment was performed. In the full scale work, P-wave vibrators were used along the ridge of Yucca Mt. (approximately 5 km line at 30 meter spacing) and 448 vertical and horizontal geophones were placed along approximately 3 km of the main drift at 15 meter spacing. Over 40,000 ray paths were collected and analyzed for P-wave energy to tomographically image the potential repository horizon and vicinity. From modeling we determined that the first arrival P-waves were mainly propagated in the Tptpmn. Tomographic inversion of the data revealed a strong correlation with fracture mapping results along the ESF. The velocity tomography results were then converted to fracture density tomograms. The results show the location and distribution of fractures over a large area of the potential repository level.

NOT APPROVED
DO NOT COPY OR DUPLICATE

1. INTRODUCTION

The primary role of geophysical studies at Yucca Mountain has been the measurement and imaging of physical rock properties. Properties such as density, conductivity, bulk and shear moduli are used to estimate other geologic properties such as stratigraphy, structure, saturation, fracturing and permeability. Although bore-holes and tunnels in the ESF (Exploratory Study Facility) will allow direct examination of physical properties, there is a need to detect and characterize subsurface features away from and between these access points. Boreholes and tunnels to date have given us a very small window into the entire repository volume. In addition, the lateral variability and heterogeneity in the Topopah formation makes it difficult to extrapolate between observation points. For example, the intensely fractured zone encountered in the ESF was not predicted. It is necessary to know the location of significant faults and fracture zones, perched water and variation in lithology and rock type to properly design and model the performance of the potential repository. It will also be necessary to understand how mining activities may affect the integrity and stability of the ESF and potential locations of the repository tunnels. Such questions as the extent of the disturbed zone, rock stability as a function of heating, and the mechanical effect of strong ground motion on the subsurface facilities need seismic data in order to be addressed.

PRELIMINARY DRAFT

The above issues were recognized and included in the planning documents such as the Pre-title II design studies. Test package 91-5 included much of the work described as part of the "Seismic tomography/vertical seismic profiling at the ESF" package. Not until the current ESF was completed, however, was there an opportunity to carry out the concept of the plans and collect data.

Also considered in the planning of this work were the results of the previous surface geophysical work carried out from 1994 through 1996 and reported in the Geophysical Synthesis effort (Majer et al, 1996, pp. 11-25). A general conclusion of this work was that the mountain as a whole was difficult to characterize from the surface due to topography variation, surface noise, near surface

weathering and lithology, as well as a variety of other access issues. By gaining access to the subsurface in the potential repository horizon we believed that one could increase the resolution as well as ground truth the results by directly observing such properties as lithology, fracture and fault patterns and relate these properties to the seismic results.

In order to meet a subset of the above needs a program to use seismic methods to image the potential repository horizon was initiated in December of 1997. Both passive and active methods were considered using ESF fracture mapping and other "ground truth" methods to calibrate and confirm the seismic methods. Such ground truthing is an important component in understanding the seismic response of bedded tuffs. The scale of applications considered varied from the meter size (i.e., damage zone investigation) up to the repository scale (imaging the volume between the ESF/ crossdrift and the surface). The program as originally planned was a phased approach that would progress as the feasibility of the methods was established and the mining of the crossdrift progressed, as well as carrying out tests once the cross drift was finished.

In addition, in May of 1998 we were asked to extend imaging beyond the original planned experiment to the south and use existing surface reflection data on Line YMP-5 to estimate the thickness and depth of the basal vitrophyre of the Topopah unit south of the potential repository region. In response to this we undertook a reprocessing of surface seismic line YMP-5 which is discussed in Section 10 of this report, and extended the tomographic analysis discussed in Section 7.

NOT APPROVED
DO NOT COPY OR DUPLICATE
PRELIMINARY DRAFT

2. Quality Assurance Status

All of the data used in this report is qualified. The tomography data was acquired by LBNL under technical implementing procedures YMP-LBNL-TIP ELM-1.0R0. Initial seismic data display was done with the seismic software package ProMAX. ProMAX is currently not qualified within the LBNL QA program, however, ProMAX processing included only sorting and displaying of data to allow identification of arrival times and amplitudes. The resulting tomographic time and amplitude data, along with source and receiver locations, is considered the acquired tomography data (DTN:LB980930123112.001) and it is qualified. Prototype experiments and data acquisition are documented in scientific notebook YMP-LBNL-ELM-1.10 and subnotebooks.

Because the geometry of the tomography survey was unique (both within and outside of YMP), modeling and analysis software was used which has not been used in YMP before. The modeling results and the software to locate the rays are not qualified. Future work should include qualification of the software. The following software was used in this report.

Software	Description	Q-Status
ProMAXv7.0:	Simple plotting and sorting:	Non-Q
Focus3Dv4.1:	General seismic processing:	Q
GXIIv2.4.1; RAY2D:	Ray Tracing:	Non-Q

FM2Dv1.0:	Wave Equation Modeling:	Non-Q
ONESTATv1.0:	Static Correction:	Q
CARTv1.0:	Tomographic Inversion:	Q
GMTv3.0; Grapher; Surfer:	Data Display:	Non-Q
EarthVisionv4.0.2:	Data Display:	Q

The programs Focus3Dv4.1, and Earth Vision are qualified. The programs CART, and ONESTAT are qualified by the receipt date of this report. The programs ProMAXv7.0, GXII, GMT, Grapher and Surfer are not qualified because they only perform data display.

The data and results in Section 10 "Reprocessing of Line YMP-5" used qualified data and qualified software (Focus3Dv4.1) for the reprocessing (Figure 19). The results of the midpoint estimation for reflection processing of surface to tunnel data (Figure 23) used GXII and is not qualified.

NOT APPROVED

3. Purpose of the Test

DO NOT COPY OR DUPLICATE

At the start of this activity there were a wide variety of needs to be filled.

PRELIMINARY DRAFT

(1.) Apply seismic methods to provide a means for broadly detecting and characterizing the following features within the potential repository vicinity: subsurface fault and fracture networks, lithologic features, and zones of perched water. There is also a critical need to extrapolate the observed fracture patterns and lithology to the surrounding regions and between bore-holes and underground workings as well as select and define structural, lithologic, and fracture domains with similar properties within the ESF. As stated above the potential repository volume has few bore-holes penetrating the horizon. If one could image the properties of the entire volume reliably between the direct observation points then valuable information could be gained to prediction geo-mechanical and hydrologic properties in this volume.

(2.) Use seismic imaging to provide a means to "look ahead" of underground workings to detect features described in (1.). If seismic methods were successful then one could have reliable means to map rock properties ahead of the tunneling so that accurate estimates could be made of time and costs of excavation. This would be valuable in the repository construction phase.

(3.) Characterize and quantify the damage associated with tunneling activities as a function of space and time through high resolution seismic imaging. If reliable engineered barriers are to be constructed, the extent of the damage zone around the tunnels must be estimated for proper design of these barriers.

(4.) Use passive seismic monitoring to predict ground motion in the underground workings from near-by seismic events. Reliable detailed seismic velocities are needed for accurate ground motion

predictions. Passive monitoring of near-by seismicity using a large array of sensors would greatly increase the amount of data (P and S wave) available for ground motion predictions.

(5.) Calibrate and relate the seismic characteristics of the host rock to the fracture patterns and lithology observed directly in the underground workings. Past geophysical work from the surface could be more closely tied to rock characteristics if more accurate velocity and attenuation models were obtained. A good example is the high resolution seismic lines over the potential repository. If more information could be derived from these data with improved velocity estimates this would improve our understanding of the subsurface.

(6.) Provide baseline measurements for performance confirmation and post closure studies. As more and more of the horizon is mined stress changes may significantly affect broad rock properties. A reliable, repeatable baseline survey may be valuable in the future to prove that significant changes have not occurred, as well as determine broad heat effects over the entire repository volume before closure.

NOT APPROVED

4. Description of Potential Tests

DO NOT COPY OR DUPLICATE

Originally three general seismic methods were considered to meet the above needs.

(1.) Cross-hole, cross-drift, drift to bore-hole, and surface to drift tomographic seismic imaging.

PRELIMINARY DRAFT

These techniques will be grouped together and can be described in general as tomographic imaging work. In these tests a seismic source is used to send energy to multiple seismic receiver positions in the above geometry. The source and receivers are moved repeatedly to give multiple seismic ray coverage from different angles in order to tomographically map a given volume of rock (Peterson, 1986, pp. 5-22). The resolution of the techniques depends upon the geometry of the survey (hole spacing, spacing of the sources and receivers and the frequency content of the seismic signals). The anticipated geometry of the surveys in the ESF could range from the scale of a few meters for mapping the tunnel damage zone (resolution of a few centimeters), to several hundred meters for imaging between the drifts (resolution of several meters), to up to kilometers for imaging the horizon as a whole (resolution of 10's of meters). Most of the tests were anticipated to be done after a section of tunnel has been mined out so not as to interfere with mining activities, however, if "look ahead" studies were to be carried out to image in front of the mining activities this would involve some halting of mining activities while the survey is being carried out.

The results of the seismic data collection from the crosshole tests would be used for tomographic imaging at several different scales; meter size, 10's of meters, 100's of meters, and up to kilometers between source and receivers. The meter size tests (such as between two boreholes drilled into the drift wall at 90 degrees to the strike of the drift) could be used to infer the damage zone associated with the tunneling and mining activities. The variation of seismic properties (velocity and amplitude of P and S waves) as a function of distance from the drift wall would be studied at various locations along the ramps where significant fracturing, and lithologic changes are encountered. Therefore these tests were not envisioned to be at equal spacing. The next larger scale surveys

were to be carried out to extrapolate and map fracture zones and other lithologic features away from the tunnel walls. These surveys were to be run between slightly larger bore-hole spacings (and tunnel to bore-hole, tunnel to tunnel) than for the damage zone studies. The spacing of the bore-holes would depend upon the feature being mapped but typical spacing of the bore-holes was to be on the order of 50 to several hundred meters apart. The 100's of meter to kilometer scale tests would be carried out between the tunnels and the surface to map the location and characteristics of the features in and around the emplacement drifts that may affect the entire potential repository integrity and ground water travel time. It was also considered to use the Tunnel Boring Machine (TBM) and or explosives from mining activities as seismic sources.

(2.) Surface to bore-hole or Vertical Seismic Profiling (VSP) (although the bore-holes may not always be vertical).

NOT APPROVED

VSP involves recording seismic energy in multiple positions in a bore-hole from a single seismic source at the surface. Sometimes multiple positions are used for the seismic sources, out and around the bore-hole. In some cases the coverage may approach tomographic density. VSP was considered to be used in exploratory bore-holes drilled from the surface to depth in front of and prior to the excavation of the exploratory ramps and shafts. VSP is relatively quick and can be performed on a non-interference basis. The resolution of the VSP techniques is up to an order of magnitude less than the subsurface tomographic imaging methods at the same scale because of the near surface highly seismic attenuating material. Therefore the resolution is expected to be on the order of 10's of meters for a VSP in a several hundred meter depth bore-hole from the surface.

DO NOT COPY OR DUPLICATE

(3.) Passive seismic monitoring in the underground workings to monitor ground motion associated with nearby seismic sources, man made and natural.

PRELIMINARY DRAFT

Within the ESF the placement of the geophones throughout the subsurface workings provides an unique opportunity to monitor the ground motion due to nearby seismic events. The concept was to use the phones emplaced for the active imaging to listen for discrete seismic events. Before the Little Skull Mt. (LSM) earthquake sequence it was assumed that regional mine blasts or testing at the Nevada Test Site (NTS) would provide the seismic energy. However, due to reduced mining and testing at NTS the most logical sources to use during the active imaging (the only time the entire array of geophones was recorded) was the seismicity from the LSM events.

5. Selection of Prototype Tests

In order to optimize and select the most effective test methods, an initial phase of investigation and prototype testing was carried out from January through April of 1998. Budget and time constraints prevented use and application of all of the above methods. Also, some of the crosshole tests described above required multiple horizontal boreholes from 10 to several hundred meters deep. Due to budget and drilling constraints this was not possible. Tests using boreholes were considered initially because optimal signal to noise and favorable geometry would be assured if a source could be placed in boreholes at the repository horizon. Proposed for use were SD-7, SD-6, and H-5, i.e. boreholes in a location such that the source-receiver ray path geometry would cross

the potential repository volume if geophones were placed in the ESF and crossdrift. Due to access problems and conflicts with other activities in the boreholes, as well as a need to have cemented casing in the sections of the boreholes being used as source boreholes, this approach was not used. In addition, the seismic tests were part of the crossdrift program to directly access the potential repository volume, thus we focused on using the ESF and crossdrift as access points rather than boreholes. This work was to be tightly coupled with and driven by crossdrift mining and results, however, as the crossdrift was delayed the focus changed to using the ESF only. Last but not least, we considered electrical methods for imaging. Although the electrical methods had shown promise, the resolution had been low. In addition, the methods had never been tried in a geometry such as this, the large amount of electrical noise and metal in the drifts, and the lack of instrumentation at the large scale (there were several seismic contractors who could provide hundreds of channels of data, but none could provide the same scale of electrical measurements) made the use of electrical methods difficult in the allotted time frame.

NOT APPROVED

Therefore, we focused on using the ESF and crossdrift as the measurements points. The general concept was to place receivers in the ESF at regular distances to record seismic energy from the surface and crossdrift. The original sequence was to first image from the surface into the ESF, predict the geology in the cross drift area, use the mapping information in the crossdrift to calibrate the seismic results, then refine and improve the image by performing tunnel to tunnel imaging between the crossdrift and the ESF. Multiple source locations along lines on the surface and the crossdrift would mimic a crossborehole geometry, thus providing data which one could process in a tomographic manner. Before we could proceed with a full scale imaging program, however, there were several unanswered questions that had to be addressed. These questions centered around the effect on seismic wave propagation of the layering and heterogeneity within the strata that was observed in the surface geophysics program. We knew that we would only have access at the surface on existing roads and drill pads. This restricted the geometry and the volume that could be imaged. The most critical issue was the strength of seismic signal that could be transmitted between the surface and the ESF. If we couldn't get relatively good arrivals we would not proceed with the program. Also, even if we did get first arrival information, could we determine the path on which these data were travelling? This was crucial to determine the location of the image. Because of these concerns, an ambitious prototype program of field measurements and modeling was undertaken to determine the feasibility of full scale repository imaging.

PRELIMINARY DRAFT

6. Prototype Field Experiments and Modeling

Two series of field tests were performed in the winter and spring of 1998. Before placing hundreds of geophones in the ESF we wanted to determine energy content and frequency range of signals generated on the surface. To do so we placed 5 three component geophones at the 3900 meter distance in the ESF. From previous experience at NTS G-tunnel we knew that how and where we placed the phones was crucial. Coupling as well as tunnel diffraction would all effect the data. Therefore, we tried several different methods of emplacing the phones. Some phones were placed in shallow vertical bore holes (approximately 6 inches deep) and secured with an approved epoxy and others with grout. Also a small horizontal shelf was chipped out on which a three component geophone could be grouted and epoxied. Another was just placed on the ground and weighted

down with sand bags. The objective was to determine the best and the most cost effective method of emplacement. These 5 phones were placed on the West side of the ESF, near the bottom of the drift, next to the tracks. In addition to these emplacements, three shallow (1/2, 1, and 2 meter), horizontal, boreholes were drilled into the East side of the drift, also for emplacing geophones. Three component phones were grouted in the end of these holes. These phones in the horizontal borehole were emplaced to record signals from explosive sources placed in shallow horizontal boreholes drilled in the south face of the North Ramp to test how much energy would be necessary to do cross tunnel imaging over the repository volume. The results of these tests will be described later. After the geophones were emplaced at the 3900 meter distance in the ESF the prototype testing began. The logistics of recording sensors in a 4 km tunnel from sources up to 5 km away on the surface were difficult, but within the ability of modern seismic systems. The signals from the geophones were digitized using the LBNL 15 channel borehole digitizer (1 ms) which is designed to work on a 4 km borehole logging cable. The signals were transmitted on a set of dedicated phone lines out to the surface where they were recorded in a vehicle sitting on Exile Hill. We chose to have the recording system outside the tunnel because in a full scale test we would not have access to the ESF. Although it was seismically quiet at 3900, fan and mining noise would interfere with the seismic data in other parts of the ESF, therefore, in a full scale test the fans and mining would be stopped, leaving no access to the subsurface during this time. The electricity in the tunnel could not be shut off due to other tests being run. We therefore had to determine if we could transmit seismic signals out of ESF reliably through the electrical noise. In addition, we had to be in radio contact with the surface sources. All of these factors made it necessary to place the recording electronics on the surface.

NOT APPROVED
DO NOT COPY OR DUPLICATE

After the geophones and recording system were put in place, we then used the LBNL vibroseis trucks to create seismic energy at the surface. In the first series of tests only P-wave (vertical vibration) vibroseis trucks were used. Three trucks were used along two previous surface seismic lines, YMP-5 and YMP-6 (Majer et al., 1996, pp. 21-22). These two lines have both seismic reflection and gravity data along them as well as access [illegible] YMP-6 was used because it was close to the repository horizon elevation (therefore close to horizontal imaging of the potential repository volume), and YMP-5 was chosen as the only other North-South access road west of the ESF and to derive information above the volume. Figure 1 shows the location of the source points and receiver used in the prototype tests. A cross section of the geometry is shown in Figure 2. As can be seen the sources along YMP-6 shoot across the Solitario Canyon Fault. Figure 3 shows the data recorded at 3900 from Line YMP-5 (Yucca Ridge) and from Line YMP-6 (Solitario Canyon). As can be seen the data from line 5 is much better than line 6 (mainly seen as better signal-to-noise ratio of the first arrivals). Due to the nature of the geometry of the survey we then tried LBNL's S-wave (horizontal vibration) vibroseis sources in Solitario Canyon. Our reasoning being that because we had nearly horizontal propagation, the radiation pattern of a vertical source would give less P-wave energy than a horizontal source, i.e., in this geometry an S-wave vibrator may give us better P-wave energy. However, this was not the case in the acquired test data, therefore we stayed with the P-wave vibrators. This is an example of how the heterogeneous nature of the subsurface requires experimental testing to validate or invalidate expectations based on simplified models.

PRELIMINARY DRAFT

The results of the prototype field tests led us to the conclusion that adequate energy could be obtained over large distances, but only on line YMP-5 was the signal-to-noise sufficient. Other

source locations, such as YMP-6 could be used if more time was allocated for repeated stacking of sources, but this would increase costs and tunnel shut-down time.

The next step was to determine if we could tell where the energy from YMP-5 was travelling and if we could use it to image the repository volume. To do so we undertook an extensive modeling effort using a full elastic 2D finite difference modeling code (FM2D) developed at LBNL as part of programs outside the Yucca Mt. Project. This code is in the process of being qualified.

The first step was to obtain a 2D velocity model. This was done by using data from the VSP collected at UZ-16 (Majer et al 1996, pp. 26-33) and projecting the velocities for the lithologic units onto a 2D cross-section of the 3D site scale geologic model (Clayton 1998, entire report). Figure 4 shows this initial velocity model. Figure 6 shows both the observed data (6a) and the initial synthetic data (6b). Although the layered model shows a fairly good waveform match to the observed data, the arrival times do not match well. Therefore, the velocity model (not geologic structure) was adjusted to better match the arrival times. After several iterations, we arrived at an acceptable match, shown in Figure 6c. The difference between modeled seismograms in Figures 6b and 6c is dramatic and shows the impact of velocity structure. Figure 5 shows the final velocity model for our cross section. The final model was a combination of adjusting the near surface velocity and having an exponential gradient in the layers rather than constant velocity. Once a model was obtained which matched the main arrivals of the prototype data, a more accurate representation of the entire wavefield (all the ESF sensors for one source) could be generated. A computed wavefield is shown in Figure 7. This time lapse sequence shows the location of the wave fronts at various times. This model clearly showed that the first arrival energy was travelling almost straight down from the ridge then travelling horizontally in the potential repository horizon. For imaging of the repository horizon this was about the best case possible, since it would provide data through a large part of the potential repository volume, imaging the desired area with a 2D geometry. We believe the initial vertical propagation is due to strong near surface velocity gradients while the later horizontal propagation is due to the relatively high velocity of the middle nonlithophysal zone. One limiting factor observed in the modeling was the long wavelength of the first arrival (about 150 m) which means the first arrival samples the upper lithophysal and lower lithophysal horizons as well as the middle nonlithophysal. This is an important point to remember for the interpretations discussed later.

NOT APPROVED
DO NOT COPY OR DUPLICATE
PRELIMINARY DRAFT

At one time it was suggested that the TBM could be used as a source for seismic energy. In order to test this concept we recorded data during the limited time the TBM was operating (it was mostly down during the prototype testing). Even with sensors as close as a few hundred meters, no usable seismic energy was recorded. We attributed it to the soft formation that the TBM was in and the high efficiency of the TBM (most the energy was going into rock breakage rather than seismic energy). Also the signal to noise ratio was poor due to the large amount of noise associated with the conveyor belt on the TBM, which served as a line source rather than a point source. If one was to use the TBM as a source then one must know the source signal for "zero" time and for source deconvolution. It appeared very difficult to do so in this case. However, because the TBM was behind schedule, we did not pursue the TBM as a source any further. There was one last prototype test performed. This was the explosive source tests in the North Ramp. If future surveys expected successful imaging to be carried out from the crossdrift to the ESF then we had to be able to have an energy source(s) that could be used in the crossdrift and be powerful enough to go the

distance. Explosives were the first choice tried. However, we were under the restriction that only limited amounts could be used, and no breakouts were allowed. It was required to direct the explosive energy into seismic energy rather than rock breakage. Because of the shallow holes provided (few meters), we were restricted to relatively small charges (1 to 2 pounds). After an initial attempt where the explosion holes were not properly sealed (the energy shot out the holes rather than into the rock) we did get off one good test. The shot hole was at 2010 and the receiver was at 3900. Over this distance a minimal amount of energy was recorded from the small charges. The tests were stopped at this point in order to focus on the surface to ESF tests. If crossdrift to ESF tests are to be done more source tests need to be carried out. Explosives could be used if larger charges are used, but due to the restriction on organic sources this is not desired. Possible sources are minivibrators and/or weight drops in the Crossdrift, nitrogen powered air guns in shallow holes instead of explosions, or if available, non organic explosive sources. Also there are many borehole seismic sources being used for crosswell seismic imaging in the oil industry, shallow (2 to 3 meter) boreholes could be used as source points for these sources. In any case the effort was stopped at that point.

NOT APPROVED

7. Final Survey Design and Execution

After completing the prototype testing, we decided that vibroseis sources on Yucca Ridge and sensors grouted in shallow holes could provide good data quality at costs within budgetary constraints. In addition to cost constraints, we needed a shutdown of tunnel activities which only happens at prescheduled times, and typically only for two days (over a weekend). Thus we planned a survey which could be completed in two days of acquisition. Among the factors affected by this time constraint were the number of source locations and the number of sweeps per source location. The prototype data had showed that 30m source spacing was a minimum to see coherent waveforms between source locations. Receiver locations had a higher fixed cost per station (including hole drilling, sensor cost, and grouting cost), but since all the sensors could be recorded simultaneously with a modern seismic recording system, there was no extra acquisition time needed for extra sensors. Therefore we decided to improve the spatial sampling by using closer sensor spacing - 15 m. This spacing also gave us better resolution at the tunnel where we would have "ground truth". In a concession to cost efficiency, we decided to use two component sensors rather that 3 component sensors. The prototype experiment and modeling had indicated that significant energy would be in the horizontal plane, but mostly normal to the strike of the tunnel. We therefore fabricated two-component (2-c) sensors (vertical and horizontal) and aligned the horizontal normal to the tunnel axis (East-West). We originally designed 170 2-c sensors, but interest and additional funding for a southern extension added 54 2-c sensors for a total of 224 sensors (448 geophones). The sensors were emplaced in the tunnel from 2680 to 5970 m. The planned source locations (including the southern extension) covered over 5000 m along Yucca Ridge at 30 m spacing. Figure 8 shows the final survey geometry in plane view.

DO NOT COPY OR DUPLICATE
PRELIMINARY DRAFT

The data recording commenced early on Saturday June 20, after the night shift of miners left and the air fans were turned off. Two vibroseis trucks were used in a linear array at each source locations (30,000 lb force each). Field testing determined the sweep parameters which were 12 second sweeps, 8 to 60 Hz, repeated 12 times at each source location. A "Varisweep" was used to

cancel the side lobes. A total of 16 seconds was recorded giving 4 seconds of correlated output. All 448 geophones were recorded for every source location. Recording progressed through Sunday June 21 until a power supply failure in the recording system ended acquisition with 19 of the 180 planned source stations not yet recorded. Repair of the recording system was not possible before the resumption of mining operations early Monday June 22. Fortunately, we had been recording every other source station, so the missing stations were interspersed with previously acquired data, thus the overall survey coverage area was not reduced. A total of 161 source stations were acquired, totalling over 71,000 seismograms. One notable observation during parameter testing was that recording during mining operations was impossible due to the high background noise (mostly from the muck conveyer belt, we believe), therefore our decision to require a tunnel shutdown was indeed necessary.

8. Data Processing:

NOT APPROVED

8.1. Sorting and Filtering

DO NOT COPY OR DUPLICATE

The data were sorted in common shot and receiver gathers. A total of 161 shots were recorded by 224 receivers. Three representative shot gathers from shot positions located at the southern, middle, and northern end of the line along the ridge are presented in Figure 9a, b, and c, respectively. The data are bandpass filtered between 20-50 Hz, while a notch filter was applied at 60 Hz. Furthermore, the data were enhanced using a 500 ms AGC window. The data are displayed for a time window of 2 s. In Figure 9a, a weak first arrival can be seen between channels 141 and 224, arriving at about 700 ms for the latter. Attenuation losses cause the amplitudes to drop below noise level for receivers located in the middle and northern end of the tunnel. A second set of arrivals can be seen at later times in the seismograms. These are P to S converted waves created at near surface interfaces. Figure 9b shows the shot gather excited in the middle of the seismic line (Source 198). It is evident that energy associated with the first arriving waves can be seen throughout the section, although they seem to be weaker for near zero offset traces. This phenomenon has been observed in surface seismic reflection studies at Yucca Mountain (Majer, et al 1996, pp. 56-59). Figure 9c shows the last shot gather for source position 280, at the northern end of the ridge. First arrivals can be seen almost throughout the whole section, which indicates that the source coupling to the ground at this source position is better, or that the near source subsurface is less attenuating, than at the southern end of the source line. The first arrival times were picked interactively for each shot gather. The data were then resorted to receiver gathers and checked and repicked for correct event identification. Event identification is an important step because a complex subsurface structure (such as at Yucca Mountain) can cause the first arriving energy to be from different raypaths than those assumed in tomography. To better understand the wave propagation in our survey, we needed a 3D elastic wave equation simulation. However such programs require long compute times and much fine tuning. Therefore we decided to use a modification of the 2D elastic program use in Section 6 to give us some insight into the 3D nature of arrivals observed in the real data.

PRELIMINARY DRAFT

8.2. 2D-3D Modeling Theory

To understand the structure and main properties of the recorded dataset as well as pick the proper arrival in the data we used a 2D elastic program with parameter adjustments allowing a simulation of 3D geometry. Such a reduction is justified for the cases of 3D problems with cylindrical symmetry where medium properties are laterally homogeneous and change just along the vertical coordinate z (i.e. horizontal layering). If we use a cylindrical coordinate system ρ,φ,z,, and place a source somewhere on Z axis then all receivers locate on a ring z=constant, ρ=constant, and with different phi are equidistant from the source. Symmetry of the problem gives the same travel times and other parameters of wavefields for all such sources. Therefore, if we know the wavefield for a vertically inhomogeneous medium for any plane containing Z axis then it is easy to expand the results for an arbitrary 3D configuration. The Yucca Mountain velocity model Exp85, which was chosen for inversion for the ridge source data, is rather close to a vertically inhomogeneous one. We used a 2D elastic code for nonuniformly spaced receivers to model receivers spaced uniformly along a line orthogonal to the model. This line represents the tunnel where the receivers were located. Therefore the correspondence between receiver location Xk in 2D model and an offset Yk of the receiver in 3D space is given by

$$X_k = \sqrt{X_0^2 + Y_k^2}$$

where Xo = 2905 ft is a zero offset distance. Such transformation allows us to make a direct comparison of moveouts of different waves on synthetic and real data. It also allows us to interpret the wave structure of the real data. Figure 9d shows modeling results for a 3D extension of our 2D final velocity model (know as Exp85). The vertical component data in Figure 9d is best compared to the right side of the acquired data in Figure 9b. Wave propagation snapshots (e.g. top of Figure 9d) was used to help identify wave types of arrivals. It was particularly clear that the direct wave has rather low amplitude and is being overtaken by reflections from the lower structures for offsets larger than about 2500 ft (see arrows on Figure 9d). Because of this result, the larger offset travel times were not used in the tomographic inversions using angles less than about 45 degrees.

NOT APPROVED
DO NOT COPY OR DUPLICATE
PRELIMINARY DRAFT

8.3. Zero Offset Analysis:

In order to have an initial estimate of the variation in seismic wave properties across the tunnel length, the data were sorted in a zero offset geometry, where the sources on the ridge were matched with opposing receivers in the tunnel. A total of 110 traces were found to satisfy this geometry and cover the total length of the geophone array. The traces alined along their first arrival travel time are displayed in Figure 10. The first arrivals can be seen at 600 ms across the zero offset gather. Is is evident that there is lateral variation in the amplitudes across the tunnel. In order to quantify this variation, the rms values of the amplitudes associated with the first arrival were determined. A time window of 80 ms (+/- 40 ms) length was applied across the first arrival and the rms amplitude values computed. The resulting values were corrected for geometrical spreading to account for losses associated with varying propagation distances. At this point the relative amplitudes can be compared across the tunnel length. To support this comparison, the fracture density, determined along the tunnel walls, is presented alongside the amplitude values in Figure 11. Both curves are normalized (the fracture density to 1, the rms amplitudes to 2) to separate them in the

plot. It is evident that the correlation is good, particularly in the sections with increased fracture intensity were the rms amplitudes rise above their background value. This result can be explained by a site amplification due to a decrease in velocity and density within the fracture zone, or by a guiding effect of the fractures which keep the propagating waves concentrated within the fracture zone, and thus prevent amplitude losses due to spherical spreading of the waves. To test the first hypothesis a noise investigation is performed. If the increase in seismic amplitudes is due to site amplification, the noise should be amplified in the same way. Therefore, the rms amplitude of the noise is determined over a 0-500 ms time window in the zero offset seismogram section. After normalization of the noise amplitudes, their values are displayed in Figure 11 (upper curve). It is clear from this comparison, that the noise is not amplified in the same way as the seismic waves, and therefore, site amplification can be ruled out as an explanation for the correlation between the seismic amplitudes and the fracture density. It is therefore likely that the intensely fractured zone encountered in the tunnel is affecting the seismic amplitudes.

NOT APPROVED

8.4. Ray Tracing:

Numerical modeling (see sections 6 and 8.2, and Figure 7) indicates that the elastic waves propagate downwards at a steep angle towards the Tptpmn zone, after which they are refracted and propagate along this interface. To accommodate this wave propagation it was necessary to project the source locations from the surface onto the top of the Tptpmn layer at depth, before 2-dimensional tomographic imaging is possible. This is a crucial step allowing tomographic imaging of Tptpmn. Since the dominant wavelength (150 m) is much longer than the layer thickness (approx. 30m) the waves sample the area immediately above and below the Tptpmn along their path to the tunnel. Wave equation modeling is poorly suited to finding specific subsurface locations where a given wave first refracts. For this reason we decided to use ray tracing to estimate the projected source locations. Additionally, we originally hoped to use a 3D ray tracer for more accurate estimation of projected source points. However, the complex velocity model made finding the correct 3D ray solutions difficult in the time available. Therefore, the projected subsurface Tptpmn source locations and associated travel time corrections were estimated by 2-dimensional ray tracing based on the final 2-D velocity model which was found through numerical modeling (section 6). After verifying the approximate projected locations with the ray tracing, a geometric calculation was made to generate the projected locations. Our application of source statics (section 8.6) corrects for any residual error from the projected source location.

DO NOT COPY DUPLICATE

PRELIMINARY DRAFT

To estimate the projected source positions within Tptpmn, ray tracing with 0.25° increments in the take-off angle was performed. The new source point is at the location where the ray that first changes from reflection to transmission intersects the Tptpmn layer in the 2D cross section. It is assumed that this point is a good representation of the location were the waves change from reflection to refraction and propagate along the interface. This location represents all rays from that source. Figure 12 shows a typical example of the raytracing result. For reasons of clarity, only an example subset of rays with take-off angles between 40° and 90° are presented. The velocity gradient causes a strong curvature of the rays, such that only a few at steep take-off angles reach the interface. The crossing point of the ray that first transmits through the layer, estimates the new source location. The raytracing was performed for all 161 source positions to estimate the locations.

The strong velocity gradient in the shallow subsurface produced unrealistically large variations in the location of the ray traced source points. We believe this is because the rays represent infinite frequency solutions to the wave equation, whereas waves with a frequency content of about f=15 Hz (as in our case) sample the medium on a larger scale. It is more likely that the true source points at depth have less variation than estimated by our ray tracing analysis. As a consequence the new source points were determined by shifting the surface locations east by the average distance of 100 m and finding their depth by projection onto the Tptpmn layer in the current geologic model.

8.5. Tomographic Imaging:

The new projected source locations and the actual receiver locations in the tunnel are shown in Figure 13, indicated by circles and triangles, respectively. This figure represents a 2D plane through the Tptpmn zone with sources and receivers projected onto it. It should be noted that the units of the coordinate system are in meters, and that the origin is located at 235191.92 m North, 170054.02 m East, in Nevada state coordinates. It can be seen that the new location of the sources are more scattered than the original locations along the ridge. The model consist of a 2-D plane, with 10m x 10m cells. Figure 14 shows the ray coverage per cell for the chosen model geometry. The ray coverage is normalized to 1, with the maximum number of rays per cell being 551. We believe that the purple colored areas (below about 10% of maximum) do not have sufficient ray coverage to provide reliable independent parameter estimates. The best sampled area lies in the center of the model, with good coverage between the center and the edges of the tunnel. It should be noted that the streakiness of the image is due to a concentration of rays along line-ups of sources in the northern and middle section of the source line. The ray coverage should be kept in mind, when the inversion results are being interpreted. Once we determined that we had good ray coverage in a 2D area, we could apply an algebraic reconstruction technique to the image area (as described in Peterson, 1986, pp. 5-22). This algorithm (implemented with the code CART) assigns each pixel a height as well as an area (hence the term 2.5D). A straight ray is drawn between the source and receiver location and the ray length through each pixel, including the height component, is calculated. The percentage of travel time (or attenuation) attributed to each pixel for each ray in that pixel is averaged by the ray path length in that pixel to give the final pixel value of velocity or attenuation.

NOT APPROVED
DO NOT COPY OR DUPLICATE
PRELIMINARY DRAFT

An initial P wave velocity tomogram is shown in Figure 14. It is apparent that the dominant features in the model are crossing line segments that extend from the lined-up sources in the northern and middle part of the source line to the edges of the receiver array. In addition strong anomalies can be seen along the southern end of the model, where the ray coverage is close to zero. These features are caused by errors in the projection of the original source positions to their new depth locations and associated travel times drifts (static shifts). The correction of these static errors for each of the new source positions became imperative to produce reliable tomographic results. A method to correct for the static shifts was applied, which is particularly suited for the current situation, where it is difficult to determine the travel time and amplitude values for every recorded trace due to the poor quality of some data traces. Contrary to the source problems, the receiver statics should be minimal, due to their grouting to the tunnel floor and the exact determination of their locations. Therefore we are confident that two component static correction (source and receiver) is possible.

8.6. Static Corrections

As stated above, the application of a stable, previously developed tomography program to the data set was validated by our modeling of wave propagation for our acquisition geometry. This analysis showed that first arrival energy propagates nearly vertically down to the Tptpmn horizon and continues laterally along that horizon. We could then extend the standard practice of near-surface (or near-borehole) static corrections to a correction for all of the propagation effects from our sources on Yucca Ridge to the Tptpmn horizon. This is a novel, but technically justified, application of static corrections which allowed the large scale imaging of the Tptpmn reported in the following section.

NOT APPROVED

We know from VSP and surface seismic results (Majer et al 1996, pp. 52-56) that seismic velocities in shallow (first few hundred meters) are very low and heterogeneous. This is usually a result of weathering , active tectonic history and other geologic processes. In addition, rocks on mountain ridges experience much lower confining pressures which allows microcracks to open and lowers velocities even more dramatically. It is our experience that the upper parts of the subsurface develop strong velocity gradients which can be found even in strong solid rock like granite. The heterogeneity of the shallow subsurface also causes the coupling of seismic sources to vary along the source line. We therefore had to remove the effect of the low velocity heterogeneous shallow velocity rocks to allow further processing. This was not unexpected because our initial numerical simulation results also suggested the presence of very low shallow velocity values. To remove this effect we must correct the travel times and amplitudes (after taking their logarithm) as having source locations (within the Tptpmn) dependent on static corrections. This was done by using a simple least square regression fit to the travel time and amplitude data (LSQR method, Pevzner et al, 1983, pp. 110-118), implemented in the program ONESTATv1.0. The present case consists of non uniform amount of data points for different source locations. We solved this problem by introducing weighting coefficients in the minimization function. Taking a data model in the form

DO NOT COPY OR DUPLICATE

PRELIMINARY DRAFT

$$u_{ij} = c_i + p\, r_{ij} + n_{ij}$$

where indexes i and j indicate sources and receivers correspondently, r_{ij} is a distance from i-th source to j-th receiver, and n_{ij} is random noise.

In the case of travel times

$$u_{ij} = t_{ij}, \quad c_i = t_i, \quad p = 1/v_0$$

where t_{ij} are travel time picks, t_i are source static corrections, and v_0 is a background velocity.

In the case of amplitudes

$$u_{ij} = \ln(A_{ij} r_{ij}), \quad c_i = \ln A_i, \quad p = -\alpha_0$$

where A_{ij} are amplitude picks, A_i are source amplitude static corrections, and α_0 is a background attenuation coefficient.

We minimize the function

$$S = \sum_{ij} (u_{ij} - c_i - p r_{ij})^2 a_{ij}$$

where coefficients a_{ij} have sense of inverse dispersions of noise defined in every data point. Thus for missing data we take $a_{ij} = 0$, and for all others $a_{ij} = 1$. Static corrections c_i as well as background parameter p are assumed to be unknown . The LSQR solution of the problem has the form

$$\hat{p} = \sum_{ij} r_{ij} a_{ij} \left(u_{ij} - \frac{\sum_{i'} u_{i'j} a_{i'j}}{\sum_{i'} a_{i'j}} \right) \bullet \left[\sum_{ij} r_{ij} a_{ij} \left(r_{ij} - \frac{\sum_{i'} r_{i'j} a_{i'j}}{\sum_{i'} a_{i'j}} \right) \right]^{-1}$$

$$\hat{c}_i = \frac{1}{\sum_j a_{ij}} \sum_j \left(u_{ij} - \hat{p} r_{ij} \right) a_{ij}$$

Note that for the case of travel times the static corrections have the sense of averaging the travel times of propagation from the ridge (source) to the Tptpmn layer. Knowing the source elevations and the distance to the Tptpmn we can calculate the effective velocities in the upper part as $\hat{v}_{ef} = d_i / t_i$. After removing the static corrections from the data the residuals are used for tomographic inversion. Figure 15 shows the static corrected velocity tomogram. Among the major features observed is a high velocity region parallel and just North of the crossdrift. The one disruption of this high velocity region is where a mapped surface fault trace intersects. A broad low velocity region is seen near the southern end of the ESF(at about 232000 N), probably associated with the intensely fractured zone, and a large low velocity anomaly is in the central southern portion of the image area at about 231800 N.

NOT APPROVED
DO NOT COPY OR DUPLICATE

Because of the high correlation of zero offset amplitudes with fracture density (USGS, Beason in the tunnel (Figure 11), we believe that seismic amplitudes may be quite sensitive to fracture properties. We therefore attempted a tomographic inversion for amplitude using the same principle of source projection to the Tptpmn horizon. The analytic solution for amplitude tomography is obtained with attenuation rather than actual amplitude values, with higher attenuation indicating lower amplitudes. The resulting amplitude tomogram is shown in Figure 16.

PRELIMINARY DRAFT

The amplitude tomograms are based on the rms amplitude values in each trace that are associated with the first arrival travel time. The rms amplitudes were determined over an 80 ms window centered about the travel time of the first arrival in each trace. The amplitude values were corrected for geometrical spreading, such that spatial comparison within the model area becomes acceptable. To help in the interpretation of these features, the relative amplitudes adjacent to the tunnel are dis-

played in a cross-sectional view along the tunnel axis and compared to the fracture distribution as presented in Figure 11. The comparison is show in Figure 17, where the tomographic amplitudes and velocities are plotted along with the fracture curve (USGS, Beason). Although the correlation is not as good as in the zero offset amplitudes, it can be seen that the amplitude maxima line up in the highly fractured section of the tunnel. We also see that the velocity structure appears to have the low frequency trends of the fracture intensity while the amplitudes have the high frequency variations. We suspect from this that the amplitude tomogram is more sensitive to local material property variations. Another notable observation is that the amplitude values appear to have positive correlation with fractures in the south end of the ESF but they have an inverse correlation with fractures in the north end of the ESF. We believe this is an indication that different material properties are affecting the amplitudes in different regions of the tomogram. This is not a surprising result since we have observed variation in material properties and localized effects which may be due to different fracture orientation, different saturation, perched water and other spatially varying features. In particular, our modeling of aligned horizontal fractures shows increasing amplitudes for horizontally propagation waves, while we know that aligned vertical fractures will cause decreasing amplitudes for horizontally propagating waves.

NOT APPROVED
DO NOT COPY OR DUPLICATE

9. Reprocessing of Surface Seismic YMP-5

PRELIMINARY DRAFT

The surface seismic reflection line along the ridge crest of Yucca Mountain, YMP-5, was reprocessed in an attempt to determine the thickness, depth, and continuity of the Vitric layer (Tptpv) at the base of the Topopah Spring Tuff (Tpt). The ridge to ESF work provided additional information on the velocity and with this information it was thought that an improved image could be obtained on YMP-5. The area of interest was the southern portion of the line, from Common Depth Point (CDP) locations 202 to 500, as shown in Figure 18.

The results from the previous processing were presented in Majer et al. (1996, pp. 11-25). In that study, four marker reflectors were found that correlate to: the Upper Topopah vitric (Tptrv); the Middle-Topopah (Tptpul-Tptpmn-Tptpll); the Lower Topopah vitric (Tptpv); and the Prow Pass (Tcp). The upper and lower vitric zones gave the strongest reflection signal, due to the dense welding of the rock, producing a greater seismic velocity contrast with the rocks above and below these vitric zones. The geologic cross-section is shown in Figure 19a. From this figure, the total thickness of the Tptrv1-3 is estimated to be about 57 meters to the south and thinning to about 38 meters to the north. All processing used the seismic processing package Focus 3D ver. 4.1, which is qualified.

In the reprocessing of the line, attention was given to the frequency content of the data. A band-limited spiking deconvolution operator was tested to retrieve the highest possible bandwidth at the zone of interest. The best bandwidth was found to be 10-60 Hertz. The stacking velocities were also re-picked; however, they varied little from the original picks. The rest of the processing flow followed the previous flow in Majer et al. (1996, pp. 12-14), including Radon velocity filtering, Stolt time migration using 70% of the stacking velocities and conversion to depth using 80% of the stacking velocities. Since no Vertical Seismic Profiling (VSP) was available on the ridge, the rock velocities at depth are not known. The conversion to depth was adjusted to match the depth of the

Tptpv units from the geologic model, which is constrained at several wells along the ridge: H-3, UZ-6, and H-5. The thickness of the individual vitric units cannot be estimated from seismic data, since the reflection could arise from any of the the three individual vitric layers and the seismic wavelength (about 100 m) can not resolve the three units. However, the seismic data can address the question of continuity of the Tptpv reflector.

The final migrated depth section is shown in Figure 19b. The upper vitric layer (Tptrv) does not appear continuous across a mapped fault at CDP 320. However, the lower vitric (Tptpv) does appear continuous at the southern portion of the line, from CDP's 202 to about 320. North of this location, the lower vitric does not appear to be as continuous, although is can be traced northward to about CDP 420, where is appears to be disturbed. Overall, the reprocessing of YMP-5 did obtain higher frequency reflections for the Tptpv vitric zone and it was found to be more continuous on the southern portion of the line.

10. Results and Conclusions:

The tomography experiment has proven to be a successful test. We demonstrated the potential of large scale, surface-to-tunnel, seismic tomography at Yucca Mountain with numerical modeling and prototype experiments. We successfully installed 224 sensors in the ESF and deployed a large scale acquisition system while mining operations were underway. We acquired a large volume of data in a short time window of mining shutdown, doing so on schedule. We developed novel techniques to maximize our imaging of the repository horizon, the Tptpmn. We have applied these techniques and produced interpretable images of over 5 square kilometers of the Tptpmn. We have produced images of two major seismic properties, velocity and attenuation. The reprocessing of the surface seismic line YMP-5 has increased confidence in the seismic interpretation of the continuity of the vitric zone.

The zero offset relative amplitude distribution revealed surprising results, in that the amplitudes are increased in regions of high fracture intensity. Having excluded a site amplification effect, one explanation may be that the horizontal fractures are guiding energy during propagation and constructively interfering to cause an increase in amplitude in a fracture zone rather than a decrease that one would expect through a highly fractured zone. In order to test this theory we performed an initial modeling exercise which confirmed the possibility of fractures inducing this result. Whether this effect is more likely for subhorizontal or vertical fractures needs investigation, but this observation holds the promise of more accurately imaging similar fracture zones. At this point the interpretation of the tomographic images is at an initial stage. There is much that could be done with further work including incorporating other material property maps based on borehole data and crossdrift data. At the time of writing, we have received no information from the crossdrift, however the possibility of constraining and testing the combined velocity and attenuation images with crossdrift results holds much promise. The combined interpretation of velocity and attenuation images is difficult. We believe that there are different physical process at work within the large area imaged. We do not expect simple agreement between velocity and attenuation, although both will define regions of material property variation. Properties such as saturation (including perched water), spatially varying velocity anisotropy, varying lithophysal content and

NOT APPROVED DO NOT COPY OR DUPLICATE DRAFT

varying fracture intensity and orientation can combine to create the observed heterogeneity. In the ESF intensely fractured zone, we have high amplitude and low velocity associated with increased fracturing. We have done initial modeling of horizontal fractures which may explain this combined result, but the modeling is not advanced enough to be used for interpretation. In other areas we expect fracturing to cause low amplitude (high attenuation) and low velocity. An example of this combination is seen just south of the crossdrift on the west side of our image.

The images themselves could be refined and improved with further work on the time picks, source projection, inclusion of receiver statics, correction for anisotropy (variation in properties with direction) and iterative forward modeling based on tomography results. While it is possible to present the velocity results in a fracture density tomogram at this point, uncertainty can be reduced with application of know methods. Nonetheless, we feel confident that the images produced can be interpreted for the following:

1) Broad regions of high velocity indicate relatively unfractured rock, such as in the blue areas of the velocity tomogram in the vicinity of the crossdrift. In this, as in past work, we feel that velocity variation within an individual formation is a good indication of fracture content.

2) Broad regions of low velocity indicate relatively fractured rock, such as in the south-central image region and along the southern end of the ESF.

NOT APPROVED

3) Subsurface faults and associated fracture zones may be defined by linear features which truncate anomalies, such as the West Ghost Dance splay which appears to truncate two attenuation anomalies between 230900 and 231900 m and also the Sundance fault mapped as crossing the crossdrift which appears to truncate velocity anomalies on the East and West sides at about 233500 m. If these observations can be corroborated with future studies, they would represent the first reliable imaging of subsurface faulting.

DO NOT COPY OR DUPLICATE

4) Attenuation appears to be more spatially variable, with good correlation of zero offset amplitudes to the mapped fracture intensity within the ESF (Figure 11). Both high and low extremes of amplitudes may indicate rock property variation such as fracturing. The amplitude data have a wider sensitivity to rock properties in general (velocities of rocks only vary at most an order of magnitude whereas amplitudes can vary several orders of magnitude).

PRELIMINARY DRAFT

5) The overall nature of the Tptpmn appears heterogeneous with fairly large velocity variation (over 20%). We note that the tomographic image does include effects from the upper lithophysal and lower lithophysal horizons and these zone are also affecting the observed heterogeneity.

In order to understand the effect of fractures on amplitude we modeled the elastic wave propagation through a homogeneous media with fractures embedded in it. In most cases we have observed that fractured zones usually exhibit high attenuation of elastic waves. This attenuation is mainly caused by intensive scattering of waves on fractures which in shallow regions have multiple orientation directions and represent sharp discontinuities in elastic properties. The case considered here, however, is different. As zero offset data show, the highly fractured zones of the ESF have strong positive correlation with amplitude of the direct waves.

To understand this phenomena we performed a numerical simulation of elastic wave propagation for the medium containing a fractured zone. The simulation was done using our elastic 2D finite difference code (FM2d). The model of the zone consisted of the 3000 ft x 500 ft region containing 100 randomly spaced horizontal "fractures" . Each "fracture" was modeled by a low (50%) velocity discontinuity having a width of one grid point (8 ft) and a length of 80 ft. For the considered wavelengths above 50 ft this is a good enough approximation for a filled fracture. A point pressure source was placed 2000 ft off the region (Figure 20a). The 21 observation points with 100 ft spacing were on a vertical profile behind the zone. A 3D display of the wave field is shown on Figure 20b where one can clearly observe an increase of the field's energy directly behind the fracture zone. An amplitude curve for the direct wave is presented on Figure 20c. As clearly seen the high amplitude region which corresponds to the zone has two low amplitude regions in the sides, which relate to trapped energy within the zone. The travel times of the wave which can be observed on Figure 20d vary smoothly, revealing negative time shifts. Therefore, the amplitudes of waves transmitted through a fracture zone are differentiated, The waveform going into the fracture zone in transformed into a more complicated wave) whereas traveltimes (velocity) are integrated and thus are smoothed. Exactly the same behavior is observed in the amplitude and traveltime tomograms, especially in the vicinity of the tunnel. This result suggests that the inhomogeneities on the tomograms can be interpreted as fracture zones. Therefore, it is reasonable to conclude that the amplitudes would be sensitive to fracture properties as indicated from the fracture modeling, however, in a tomographic sense we have not had the opportunity to derive a fracture tomogram which includes amplitude effects. The difficulty being that as the angle of incidence of the seismic waves varies relative to the fracture plane the fracture may attenuate or amplify the energy (as seen in the modeling in Figure 20) Thus without proper correction for angle of incidence the amplitude images should be looked at as only a general indication of fracture location.

NOT APPROVED

In an attempt to understand the anisotropy effect, we derived amplitude and velocity tomograms with different ray angles, reasoning that if the tomograms with only low angles of incidence looked different from those with only high angles of incidence, then anisotropy is playing a significant role. Plotted in Figure 21a, b, c, and d are the velocity tomogram with rays of 30 degrees and less, 45 degrees and less, the amplitude tomograms with rays of 30 degrees and less and 45degrees and less, respectively. Although the tomograms in Figure 21 do look different in fine scale detail from the tomograms with all of the rays (compare to figures 15 and 16), the broad features are the same. In fact the tomograms with ray angles less than 45 degrees are a more robust measure of the overall broad features than the tomograms with all of the rays. This is because we used a straight ray inversion for the tomography, ignoring bending. If there are strong velocity gradients in the area (which there are) then the high angle rays across the gradients will bend and not be as well approximated by straight rays.

DO NOT COPY OR DUPLICATE

PRELIMINARY DRAFT

In an attempt to quantify the fracture properties, we used a relationship between seismic velocity (P and S-wave), fracture density, matrix properties, and fluid saturation which was derived by Kaelin (1998, pp. 64-80). We successfully applied this to the UZ-16 VSP data (Majer et al, 1996, pp. 8-11) to derive the saturation and fracture density profile, but unlike the ESF, UZ-16 had no confirmation of large scale fracture density which was affecting seismic wave propagation within the wavelengths generated by the VSP. The accuracy of our results at UZ-16 demonstrated the applicability of the theory to the nonlithophysal and lithophysal stratigraphy. Shown in Figure 22 is a tomogram of the fracture density. Unlike the data from UZ-16, there are many assumptions used to

derive this figure. We assumed an average Poisson's ratio of 0.34 for the unfractured matrix, an average crack saturation of 60%, an S-wave velocity of 2150 m/s (we have not developed an S-wave tomogram or even picked the S-wave yet) and used the matrix properties of core (such as Poisson's ratio) from UZ-16 for the Tptpnm mineralogy. We also assumed all porosity is fracture porosity (total porosity in the Tptpmn is about 10%). Additionally, we assumed that the fractures had an average dimension of 1 square meter. All these values were fixed throughout the imaged volume. We know that these properties vary throughout the imaged volume, however it is not within the scope of this report to include other laterally varying properties. We should note that with S-wave velocities (possibly pickable from our tomographic data set) and a better estimate of saturation and porosity (possibly from the UZ site model, or interpolated log data), a more accurate estimate of fracture density throughout the imaged area could be derived. The information from the attenuation tomogram was not used. We have also not attempted to normalize to the mapped fracture density in the ESF. As can be seen the results match quite closely to the measured values along the ESF, providing confidence that seismic velocity correlated closely to fracture properties. Further refinements of the fracture density could be obtained by more accurate values of saturation, S-wave velocity and matrix properties.

NOT APPROVED

11. Future Work

DO NOT COPY OR DUPLICATE

In order to extract the most information from the current data set future work should include improving and refining the current tomographic data set and exploiting the knowledge gained here to address the questions described in Section 3. The current data set would benefit from the following:

PRELIMINARY DRAFT

1) Forward modeling for understanding the relationship between velocity and attenuation in various settings (i.e. fractured vs. nonfractured, saturated vs. dry fractures, horizontal vs. vertical fractures, etc). Forward modeling using the inverted tomographic velocity image would also study the velocity structure effect on amplitudes (such as focusing of energy by spatial velocity variations).

2) Design and application of receiver statics

3) Analysis for anisotropy, including spatially varying anisotropy

4) Correction to amplitudes based on "focusing" of the velocity model (beyond straight ray tomography)

5) Inclusion of S-wave data to derive more robust estimates of fracture properties, this will require more modeling to identify the S-wave in our data (versus converted and more complex arrivals). To date we have not been able to pick the S-wave over the data set due to the complexity of the wave field. In addition, if we correlated with the saturation properties that Rautman (Rautman and McKenna, 1997, pp. 87-134) has derived this also may derive a more robust estimate of fracture properties.

6) Acquire cross drift to ESF data sets to have a wider band width data set in order to interpret the amplitude data in terms of fracture properties. A higher resolution image using subsurface sources as well as receivers would also greatly aid in further refinement of the fracture properties.

Future work could utilize the permanently emplaced ESF geophones, as well as the knowledge gained about velocity and attenuation variation in the Tptpmn. Because the geophones are already in place the following work could be done:

1) Collect passive seismic data to image beneath the potential repository volume as well as refine the P and S-wave velocity model for earthquake hazard predictions.

2) Perform another survey similar to the one carried out with a source line to the East of the ESF (possibly along seismic reflection line YMP-2, the road to the south portal). This would image the zone to the east of the ESF, an area where we have many more boreholes and confirming information, thus if we imaged the fracture zones properly in that region, we would have much more confidence in our current results. It would also provide an interesting comparison between a zone rejected as a potential repository to one still being considered for the potential repository.

NOT APPROVED

3) Tunnel reflection studies

Future work of the tomographic data could include processing for reflected energy. In anticipation of this, some modeling was performed to determine the area that could be imaged from the reflection points off the lower vitric layer of the Topopah Spring Tuff (Tptpv). The modeling program used was GXII ver. 2.4.1, which is in the process of being qualified. This is a ray tracing program that has the option to export the location of reflected midpoints.

DO NOT COPY OR DUPLICATE

PRELIMINARY DRAFT

In this modeling, a 2-D velocity model was constructed following the methods described earlier that simulate the 3-D case (see Section 8.2). The velocity model used was similar to the Final Velocity Model (Figure 5), except that an exponential function could not be used in GXII that started from ground level. Instead, a slow velocity of 914.41 m/s was assigned to the first layer (Tiva) so that the first arrival times matched the observed. The rest of the layers were 85% of the Original Velocity Model (Figure 4), as was the case with the Final Velocity Model.

The midpoint reflection locations were calculated for one 2-D model, and then rotated to the 3-D case, as described in Section 8.2. Additional shots were added based on the shot-receiver geometry, and the results are shown in Figure 23. This plot shows the location of the reflection points from the lower vitric, Tptpv. As can be seen, they form a rather narrow band between the shots and receivers. The band is so narrow because the fast velocities in the Tptpmn layer above it (see Figure 23) tend to focus the reflected rays vertically. Thus, large areas of the Tptpv are not sampled by the reflections; however, smaller areas tend to be highly sampled.

4) Tunnel to Tunnel Reflection Imaging

The subsurface access provided by the ESF and other future drifts allows the possible use of high resolution reflection profiling for horizons below, and possibly above, the tunnel. As a preliminary investigation of the potential to image below the ESF with reflection profiling, we performed wave

equation modeling for a source and receiver in the ESF on the 2D cross section of our final velocity model. This modeling is shown in Figure 24. We found a complex wavefield (as expected) with P-wave reflections from above and below the tunnel as well as P to S-Wave conversions. The horizon which seems to be best imaged (because of reflection amplitude and time separation from other arrivals) is the basal reflector of the Calico Hills formation (Ta). Figure 24 shows time snapshots of the wave propagation as well as a synthetic seismogram for horizontal and vertical component receivers in the ESF. The reflecting energy from the base of Calico Hills would be affected by internal Calico Hills properties both going down and coming up, thereby increasing the sensitivity. If the Tptrv reflector could be resolved, then we could also define the approximate thickness of the Calico Hills formation.

NOT APPROVED

REFERENCES:

CRWMS M&O. 1998. Clayton, R.W. A 3-D Geologic Framework and Integrated Site Sub-Model (GFM3.0) of Yucca Mountain, Nevada. DTN: MO9804MWDGFM03.001 (NQ).

CRWMS M&O. 1997. Clayton, R.W.; Zelinski, W.P.; and Rautman, C.A. ISM2.0: A 3D Geologic Framework and Integrated Site Model of Yucca Mountain. B00000000-01717-5700-00004. MOL.19970122.0053. DTN: MO9807MWDGFM02.000 (NQ)

Kaelin, B. 1998. Seismic Imaging of the Shallow Subsurface with High Frequency Seismic Measurements. LBNL Report 42058, Ph.D Thesis. Berkeley, California: Lawrence Berkeley National Laboratory. ACCN: to be determined.

Majer, E.L.;Feighner, M.A.; Johnson, L.; Daley, T.; Karageorgi, E.; Lee, K.H.; Williams, K.; McEvilly, T. 1996. "Synthesis of Borehole and Surface Geophysical Studies at Yucca Mountain, Nevada and Vicinity", Surface Geophysics, 1. Milestone Report OB05M. Berkeley, California: Lawrence Berkeley National Laboratory. MOL.19970716.0308.

Peterson, J. E. 1986. The Application of Algebraic Reconstruction Techniques to Geophysical Problems. Ph.D. Thesis, LBL-21498. Berkeley, California: Lawrence Berkeley National Laboratory. TIC: 239765.

Pevzner L. A.; Kovtun A. A.; and Korneev V.A. 1983. Usage of One-Hole Seismic Cross-Lighting Data for Investigating of Mineral Deposits – Problems of Dynamic Theory of Seismic Waves Propagation, 23. Nauka, Leningrad. ACCN: to be determined.

Rautman, C.A. and McKenna, S.A. 1997. Three-Dimensional Hydrological and Thermal Property Models of Yucca Mountain, Nevada. SAND97-1730. Albuquerque, New Mexico: Sandia National Laboratories. MOL.19980311.0317.

USGS, S. Beason, Fracture Data, ESF Station; DTN as follows:
0+60—4+00; GS971108314224.020
4+00—8+00; GS971108314224.021

DO NOT COPY OR DUPLICATE
PRELIMINARY DRAFT

8+00—10+00; GS971108314224.022
10+00—18+00; GS971108314224.023
18+00—26+00; GS971108314224.024
26+00—30+00; GS971108314224.025
30+00—35+00; GS960708314224.008
35+00—40+00; GS960808314224.011
40+00—45+00; GS960708314224.010
45+00—50+00; GS971108314224.026
50+00—55+00; GS960908314224.014
55+00—60+00; GS971108314224.028
60+00—65+00; GS970208314224.003
65+00—70+00; GS970808314224.008
70+00—75+00; GS970808314224.010
75+00—78+77; GS970808314224.012

NOT APPROVED

DO NOT COPY OR
DUPLICATE

PRELIMINARY DRAFT

NOT APPROVED

DO NOT COPY OR DUPLICATE

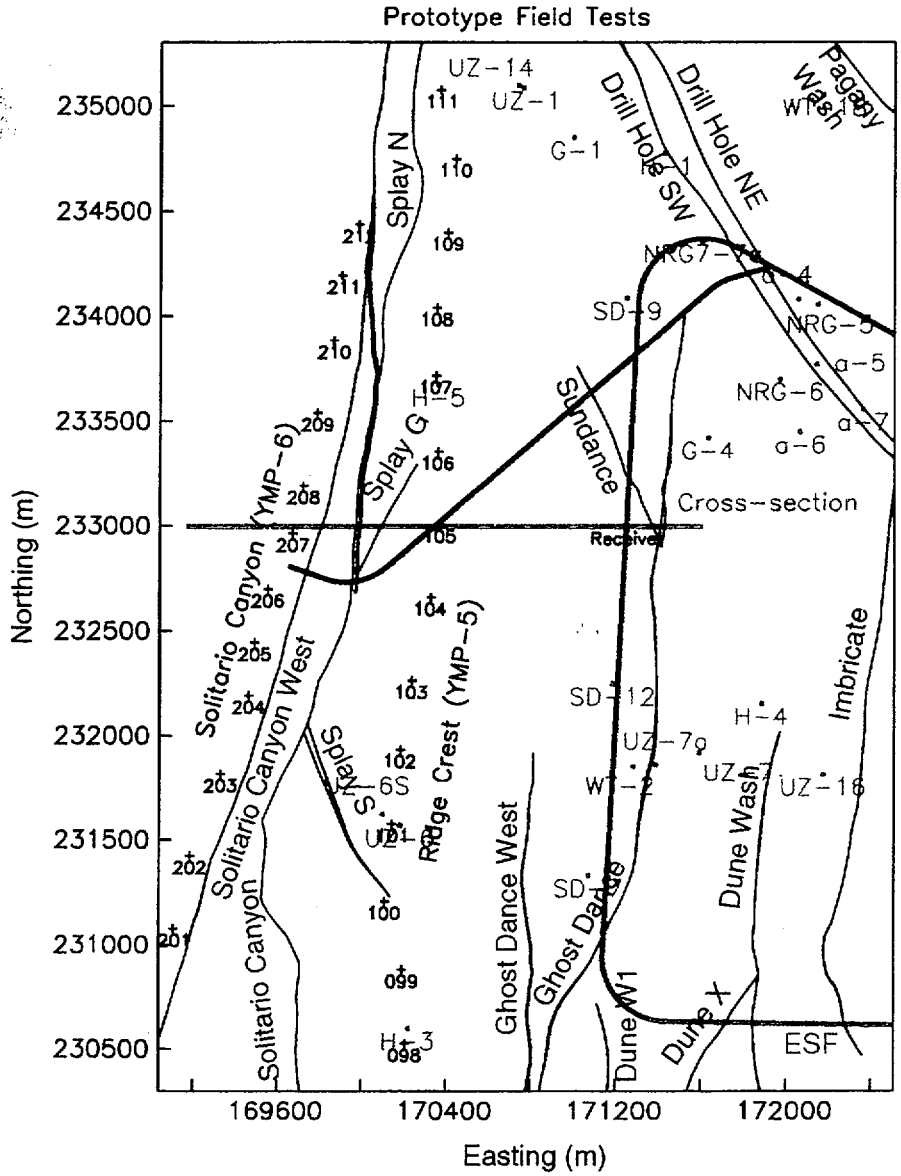

Figure 1 Source and receiver location for the tomography prototype testing. Source sites on Yucca Ridge are labeled 098 - 111. Source Sites in Solitario Canyon are labeled 201 - 212. The sensor location in the ESF is labeled "Receiver". The ESF and crossdrift tunnels are in blue and major faults are in red. Coordinate scales are in Nevada state plane in meters. The green line shows the cross section location of the geologic section (Figure 2) and the velocity model (Figure 5). DTN:LB980930123112.001 and Clayton, 1998.

PRELIMINARY DRAFT

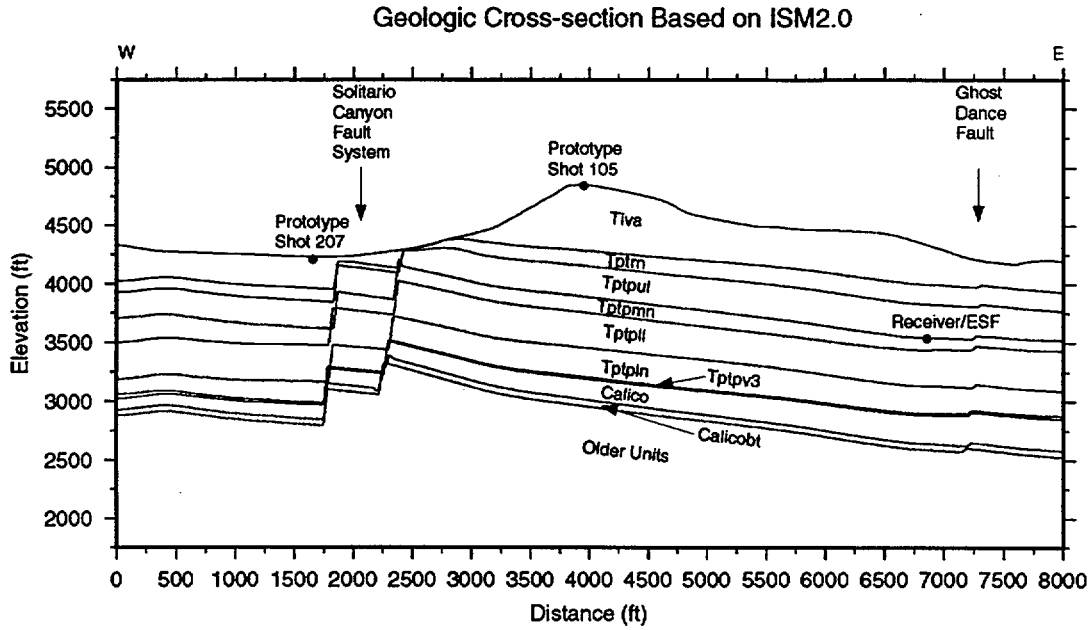

Figure 2 Geologic cross section used for 2D modeling. The geology comes from the 3D site scale model ISM2.1. Clayton, 1998.

DO NOT COPY OR DUPLICATE

NOT APPROVED

PRELIMINARY DRAFT

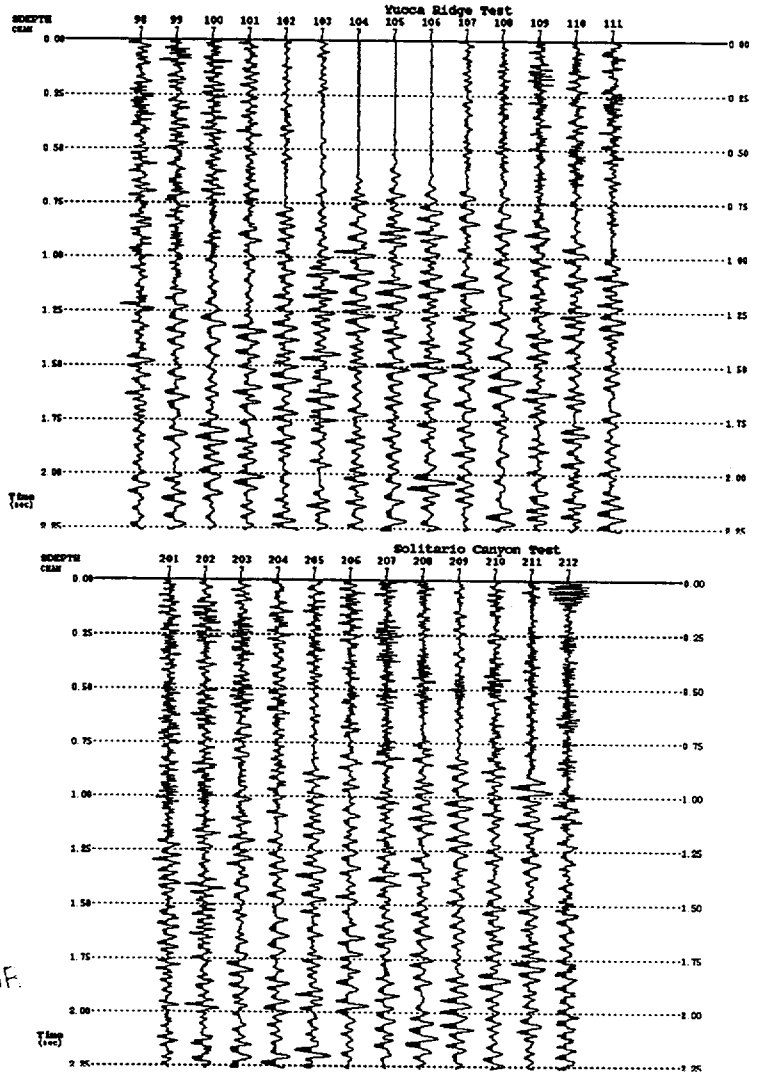

DO NOT COPY OR DUPLICATE

Figure 3 Common receiver gather data from prototype experiments. Data is from P-wave sources on Yucca Ridge (top) and Solitario Canyon (bottom). There is a notable difference in signal-to-noise ratio of the first arrivals. (DTN:LB980930123112.001)

NOT APPROVED

PRELIMINARY DRAFT

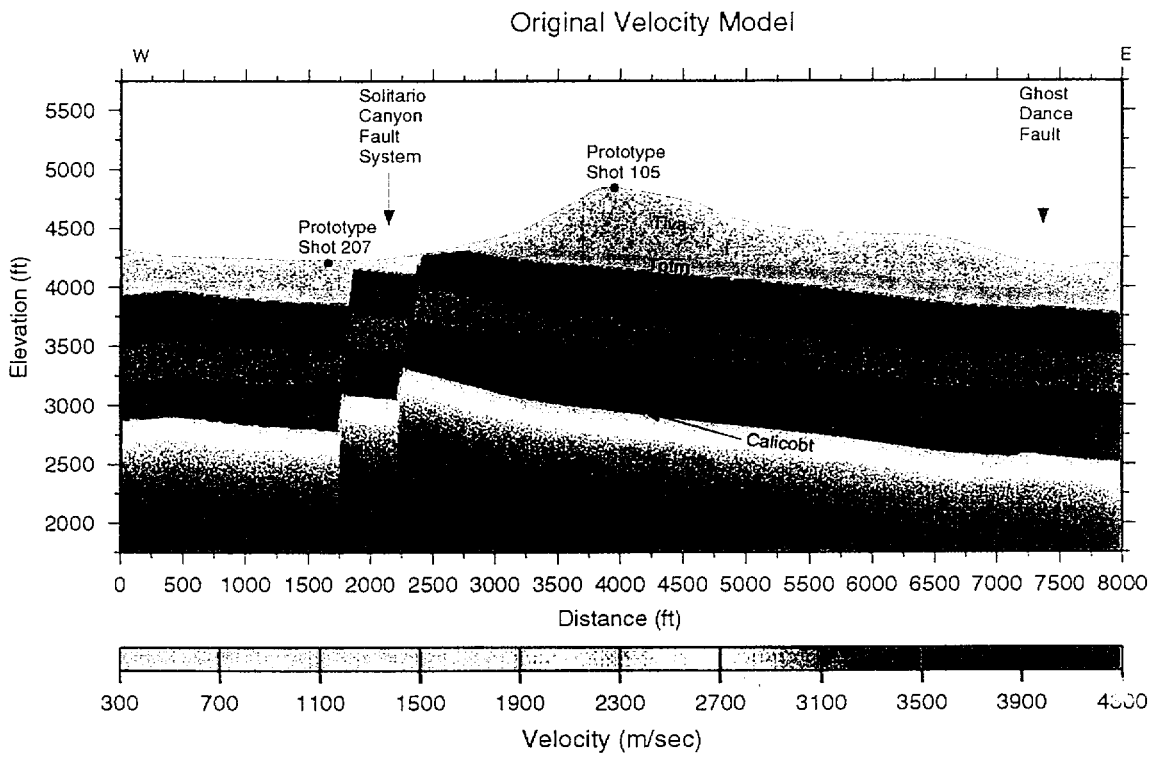

Figure 4 Starting velocity model used for analysis of prototype experiment. Geologic cross section is same as Figure 2. Clayton 1998.

NOT APPROVED

DO NOT COPY OR DUPLICATE

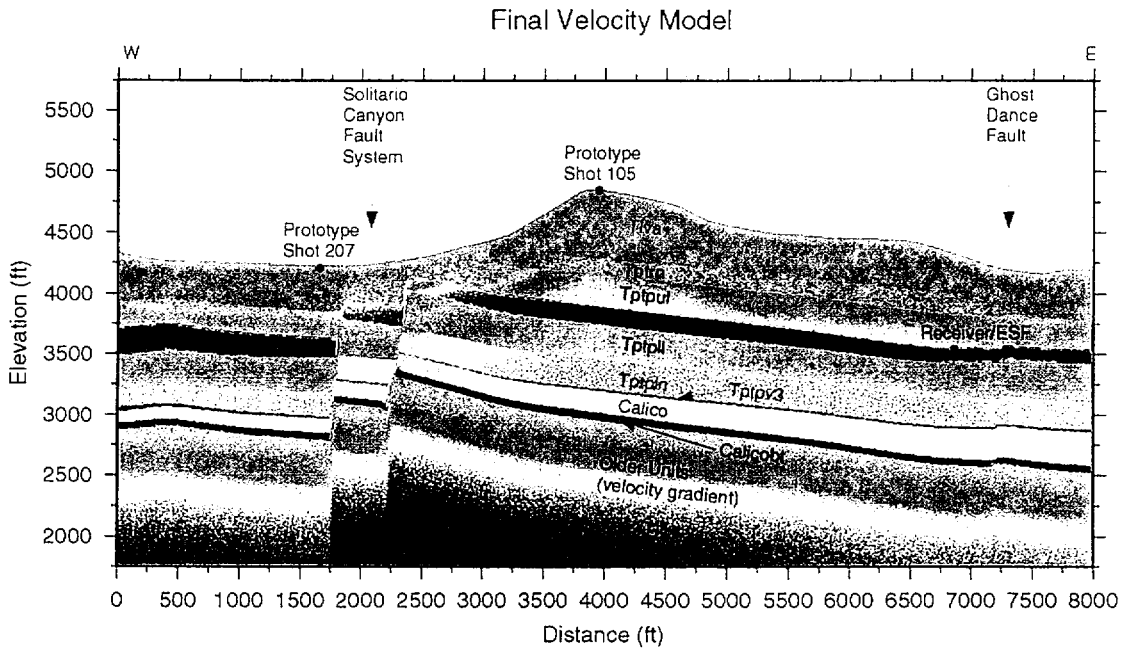

Figure 5 Final velocity model used for analysis of prototype experiment, wave equation modeling and ray tracing for tomography projected source location. Geology from Clayton, 1998.

NOT APPROVED
PRELIMINARY DRAFT
DO NOT COPY OR DUPLICATE

Search of background velocity model for Yucca Mountain using numerical modeling for a source at Ridge

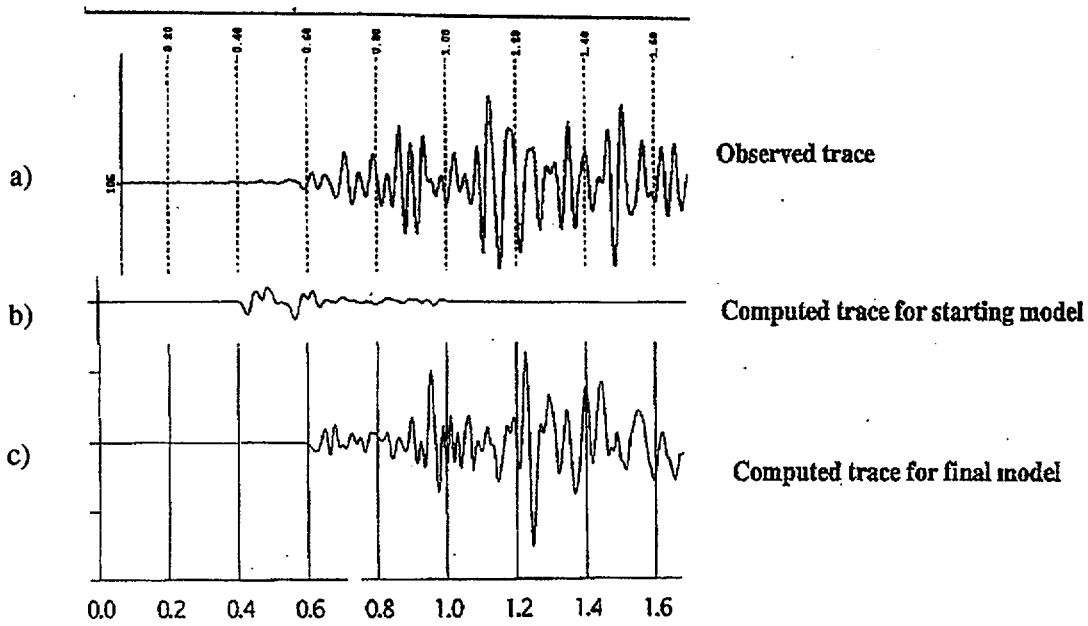

Figure 6

Comparison of observed and modeled data for the prototype experiment. 6a(top) is the seismogram for source site 105 (on Yucca Ridge) and a sensor in the ESF. 6b (middle) is a synthetic seismogram calculated using the starting velocity model shown in Figure 5. 6c (bottom) is a synthetic seismogram calculated using the final model. While the final model is not a perfect match, it has much improved agreement in arrival time and waveforms.

NOT APPROVED

DO NOT COPY OR DUPLICATE

NOT APPROVED

Seismic wave propagation for Yucca Mountain with vertical source on the Ridge

DO NOT COPY OR DUPLICATE

PRELIMINARY DRAFT

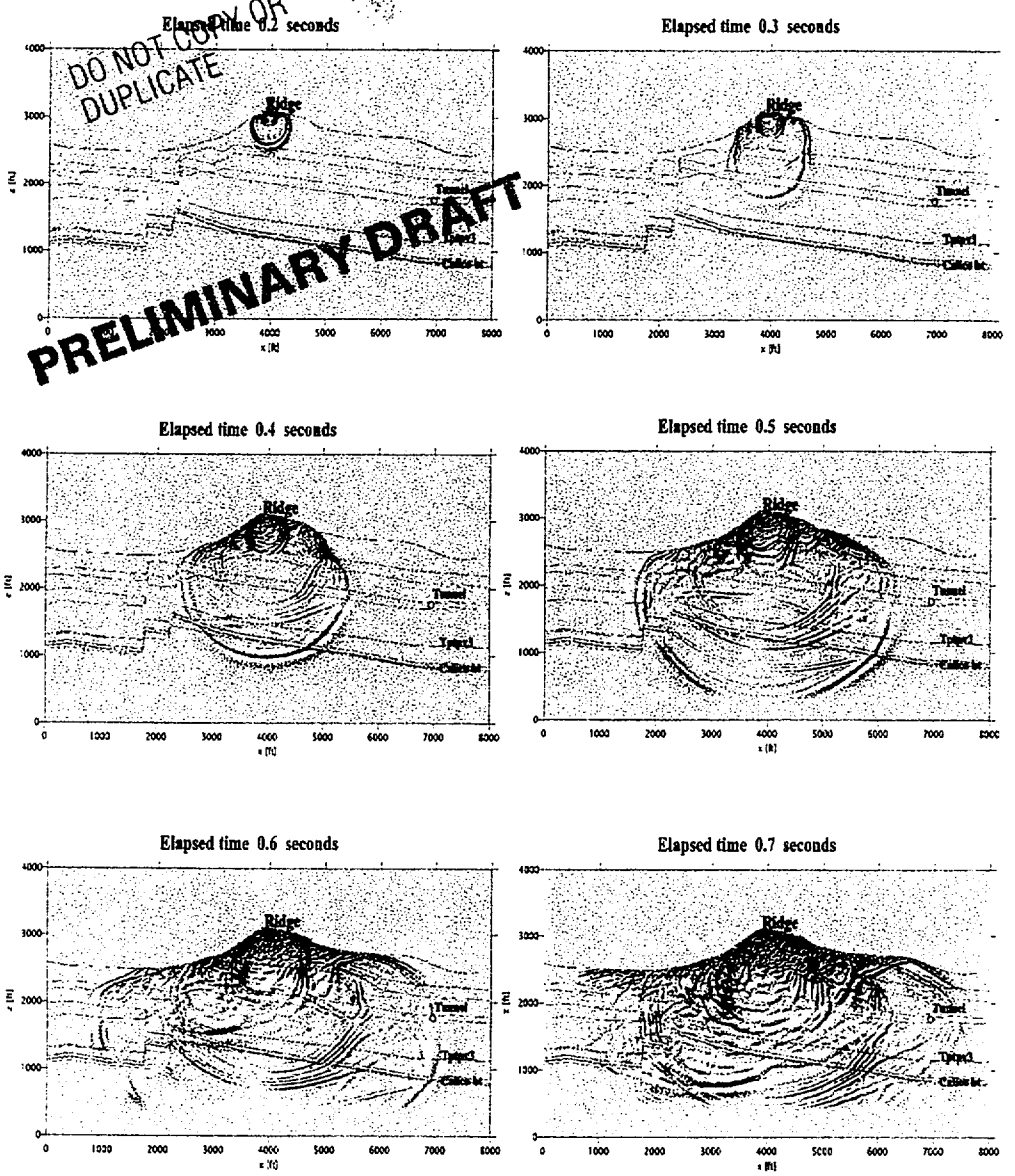

Figure 7 Sequential time snapshots of wave propagation modeling in the final velocity model. Note that in the 0.3 second frame (top right) the direct P-wave has already reach the tunnel horizon with little lateral propagation. In the 0.4, 0.5 and 0.6 second frames, the initial wave continues to propagate in the tunnel horizon. It is this observation which justifies our use of 2D tomographic imaging. Other attributes of this modeling are discussed in the text.

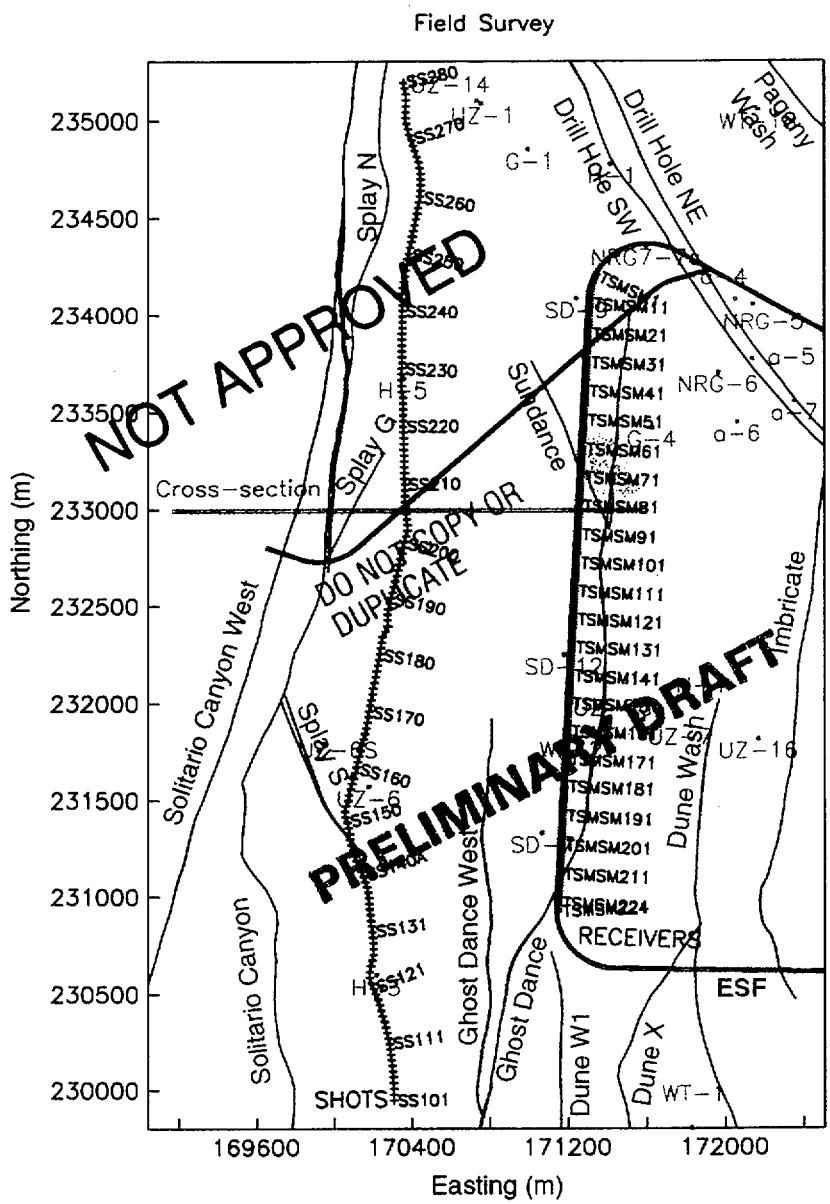

Figure 8 Location of sources and receivers for the full scale tomography field experiment. The source location are labeled SS101 to SS280, the receiver locations are labeled TSMSM101 to TSMSM224. The ESF and crossdrift tunnels are shown in blue, major faults are in red and the 2D model cross section is in green. Coordinate scales are in Nevada state plane in meters. DTN:LB980930123112.001 and Clayton, 1998.

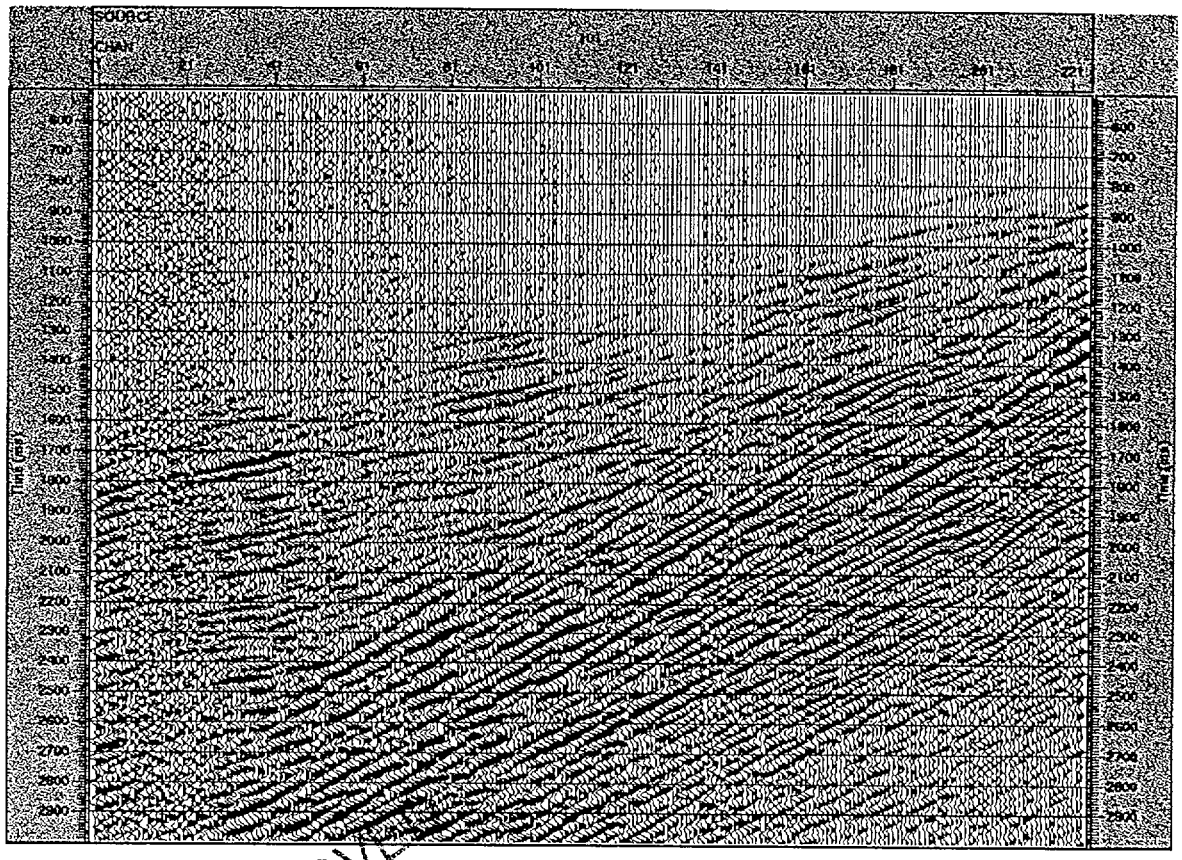

Figure 9a. Common shot gathers of the z-component for Source Location 101 (x=253.0m, y=5246.0m, z=-31.51m) along the Yucca Mountain ridge.

NOT APPROVED
DO NOT COPY OR DUPLICATE
PRELIMINARY DRAFT

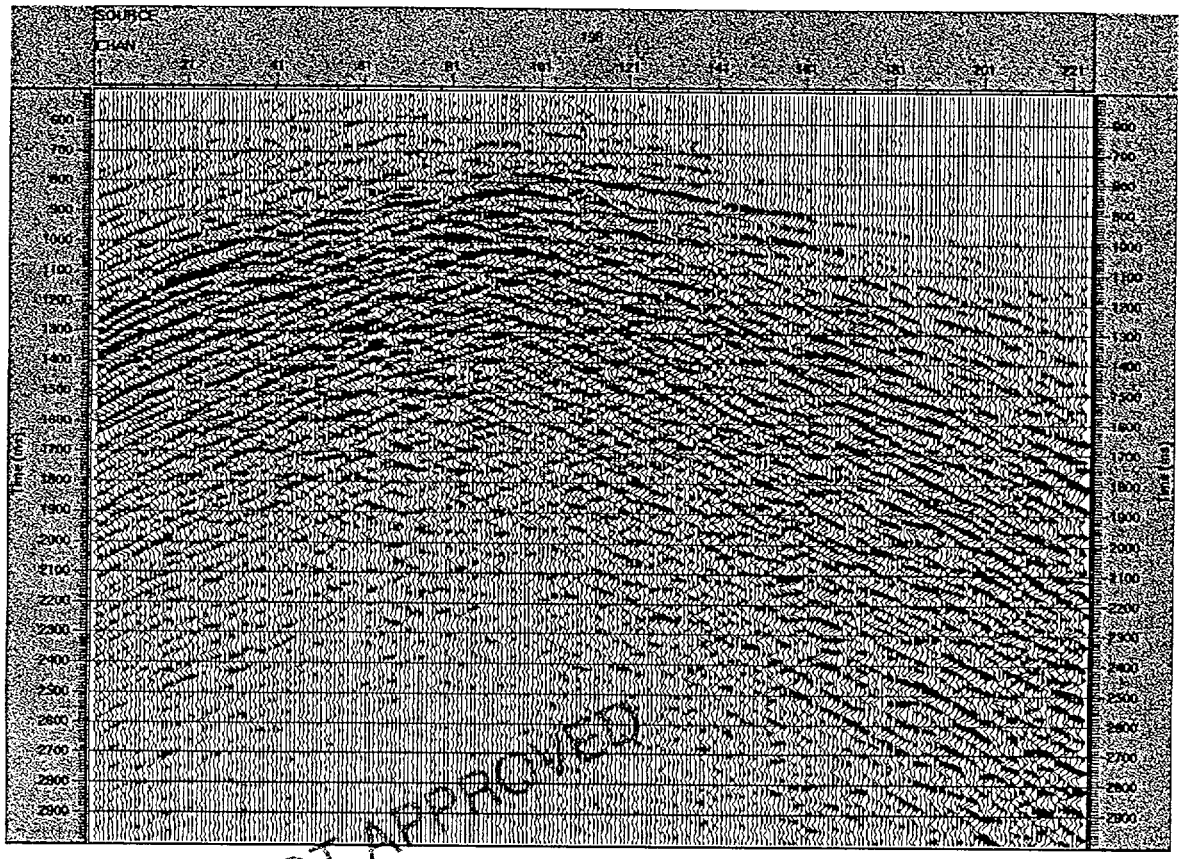

Figure 9b. Common shot gathers of the z-component for Source Location 198 (x=295.0m, y=2737.0m, z=-13.03m) along the Yucca Mountain ridge.

NOT APPROVED
DO NOT COPY OR DUPLICATE
PRELIMINARY DRAFT

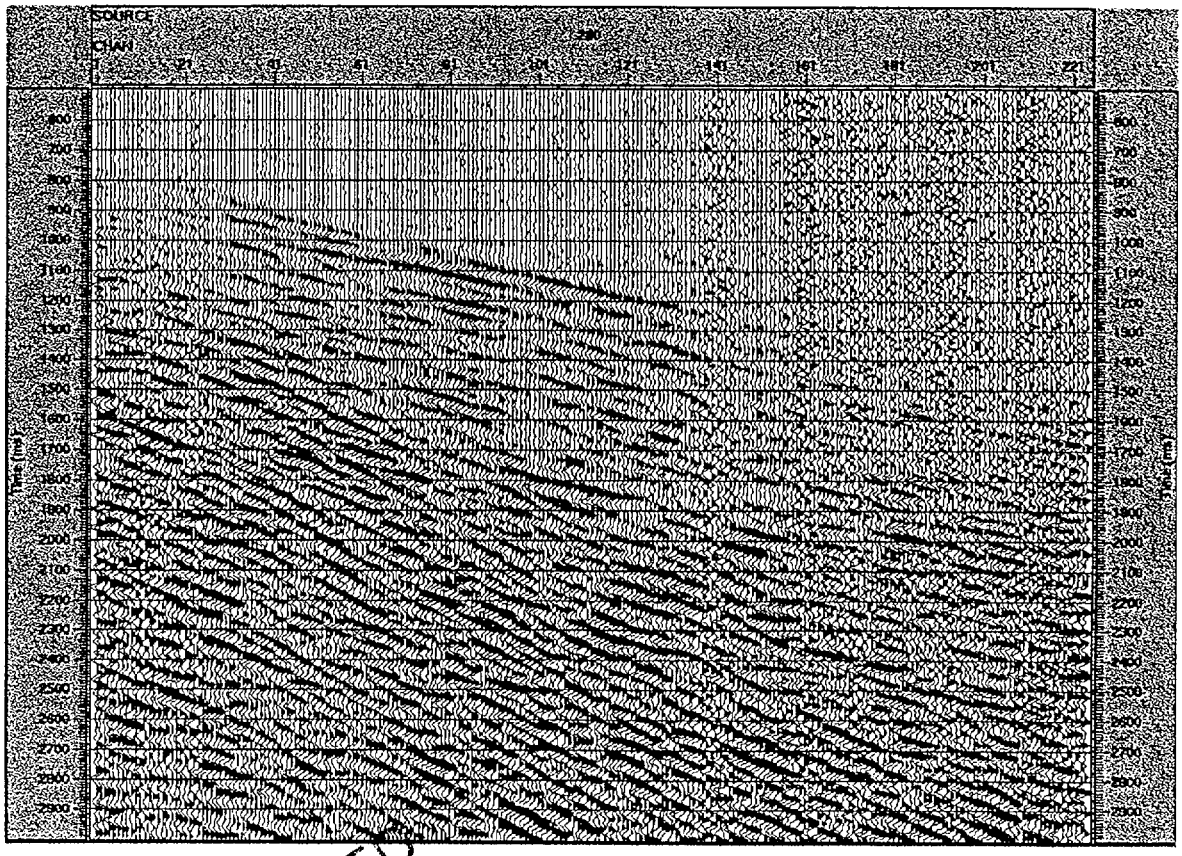

Figure 9c. Common shot gathers of the z-component for Source Location 280 (x=301.0m, y=0.0m, z=-26.85.03m) along the Yucca Mountain ridge.

NOT APPROVED
DO NOT COPY OR DUPLICATE
PRELIMINARY DRAFT

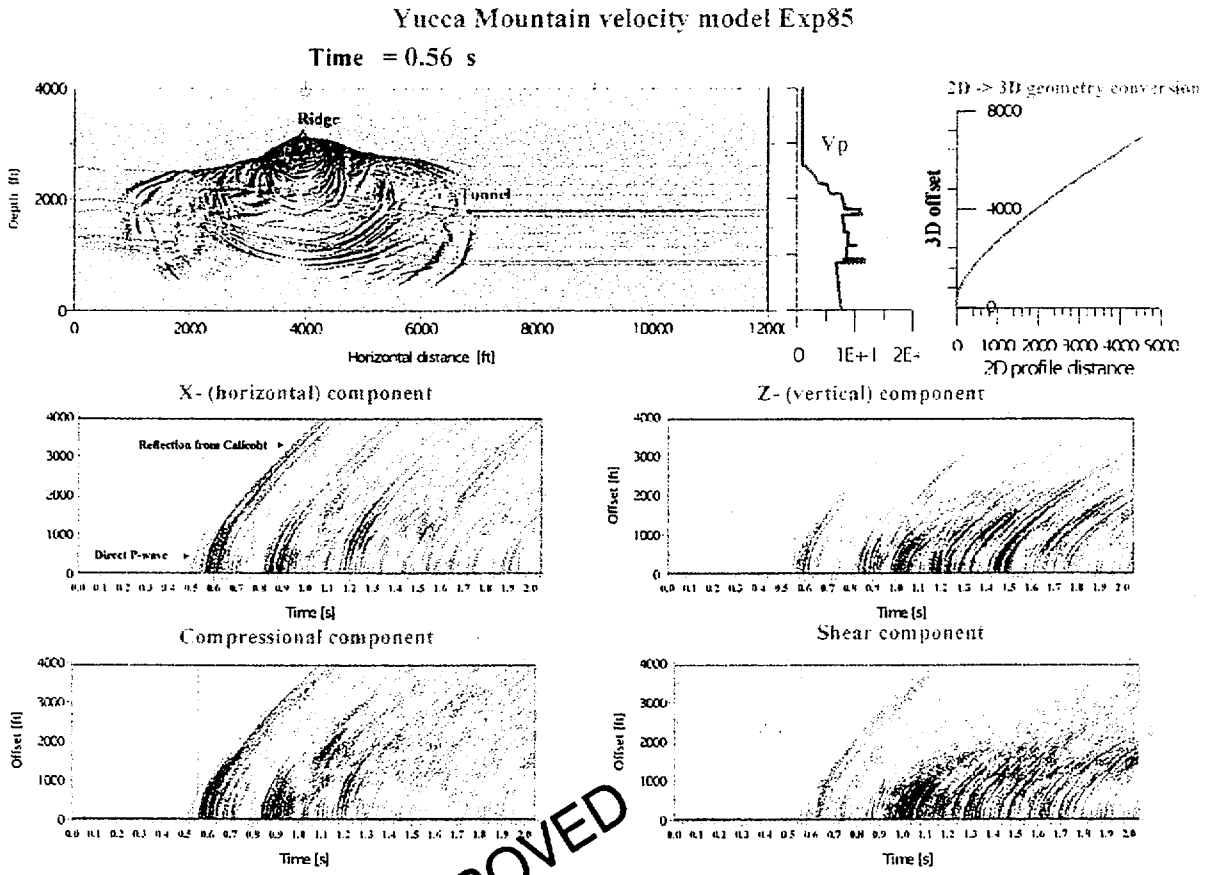

Figure 9d. 3D-2D modeling of source gather showing time snapshot and synthetic seismograms.

NOT APPROVED

DO NOT COPY OR DUPLICATE

PRELIMINARY DRAFT

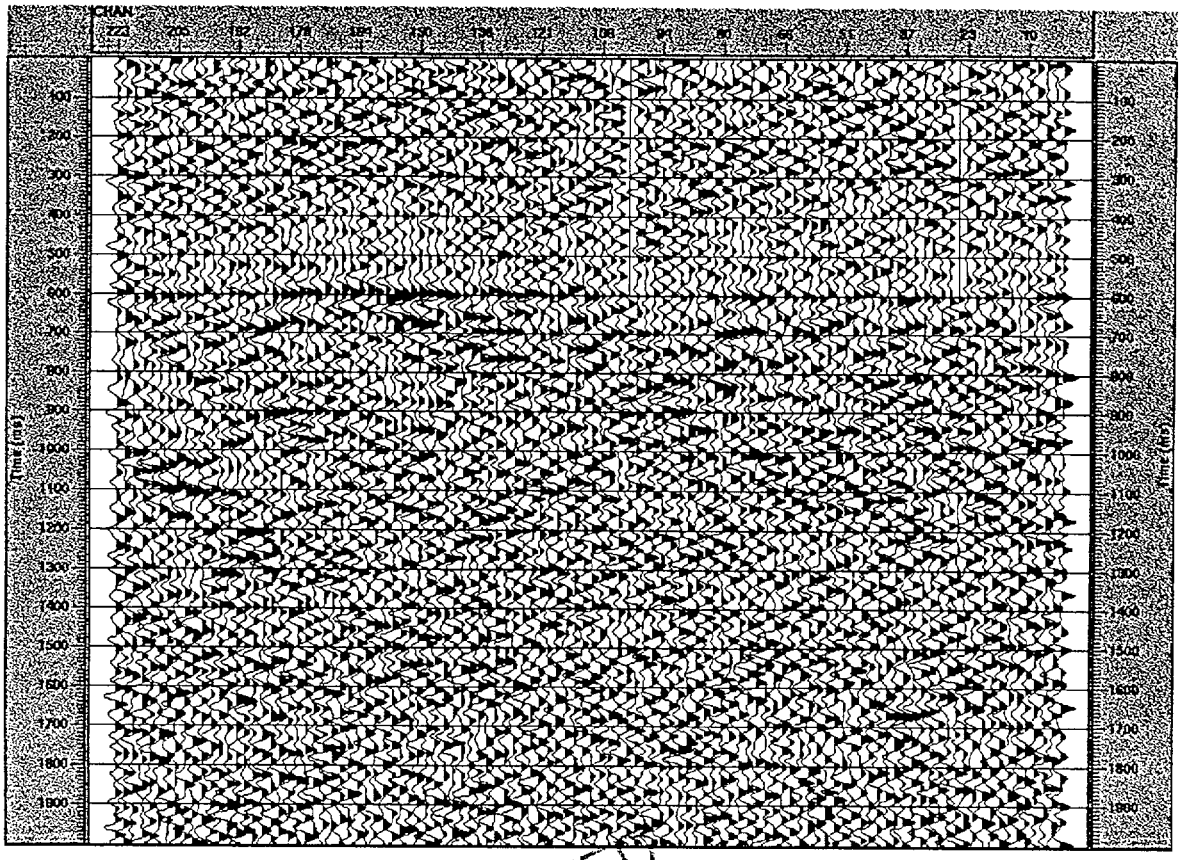

Figure 10. Zero offset gather (z-component) for opposing source receiver pairs. First arrivals are aligned at t=600ms. (DTN:LB980930123112.001)

NOT APPROVED
DO NOT COPY OR DUPLICATE
PRELIMINARY DRAFT

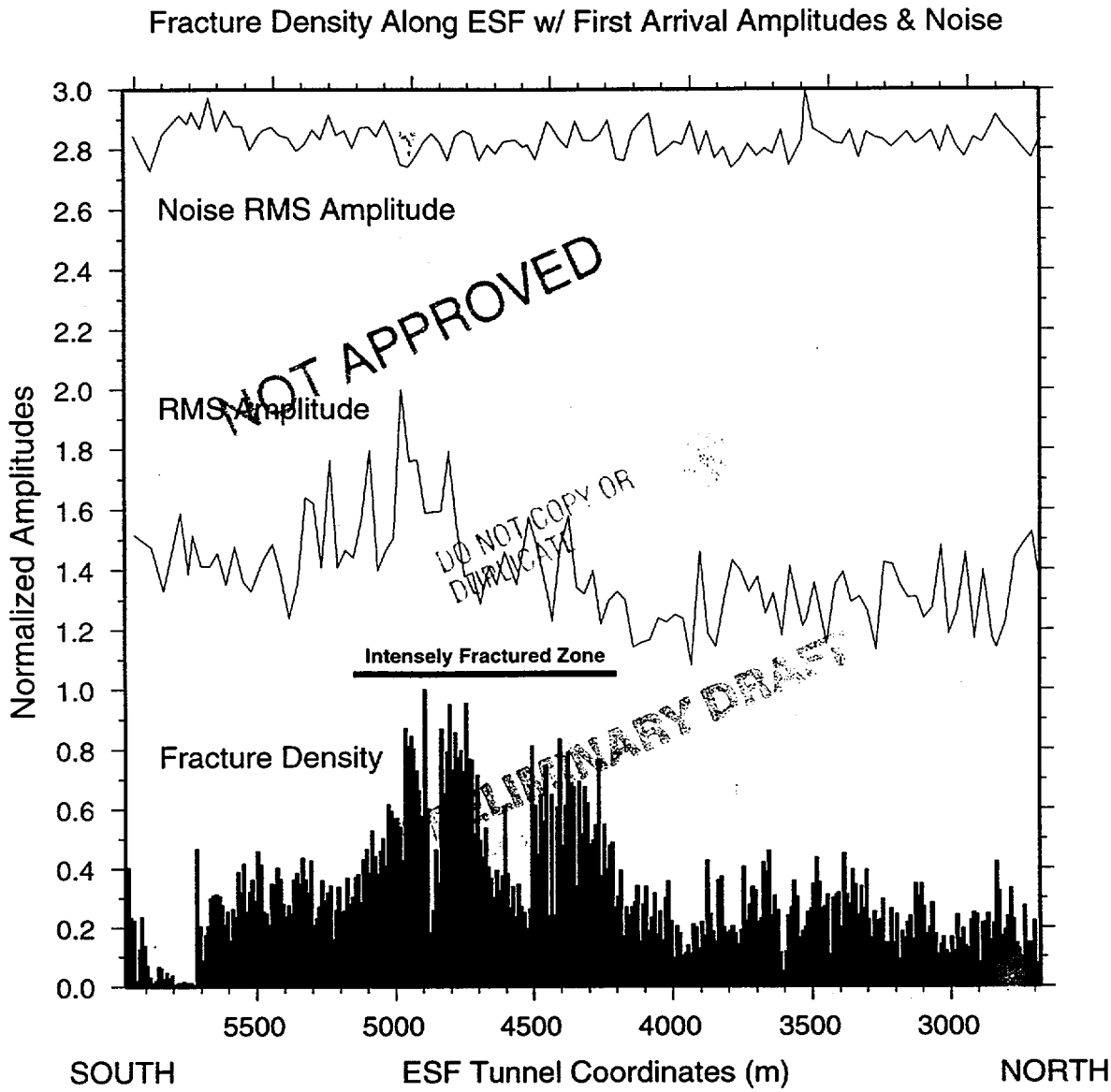

NOT APPROVED
DO NOT COPY OR DUPLICATE
PRELIMINARY DRAFT

Figure 11. First arrival RMS amplitude values as a function of location in the tunnel. RMS amplitude of first arrival (middle curve), fracture density as measured inside the tunnel (lower curve). RMS amplitude of 500 ms noise window (upper curve), fracture density as measured inside tunnel (lower curve), (USGS, Beason). (DTN:LB980930123112.001)

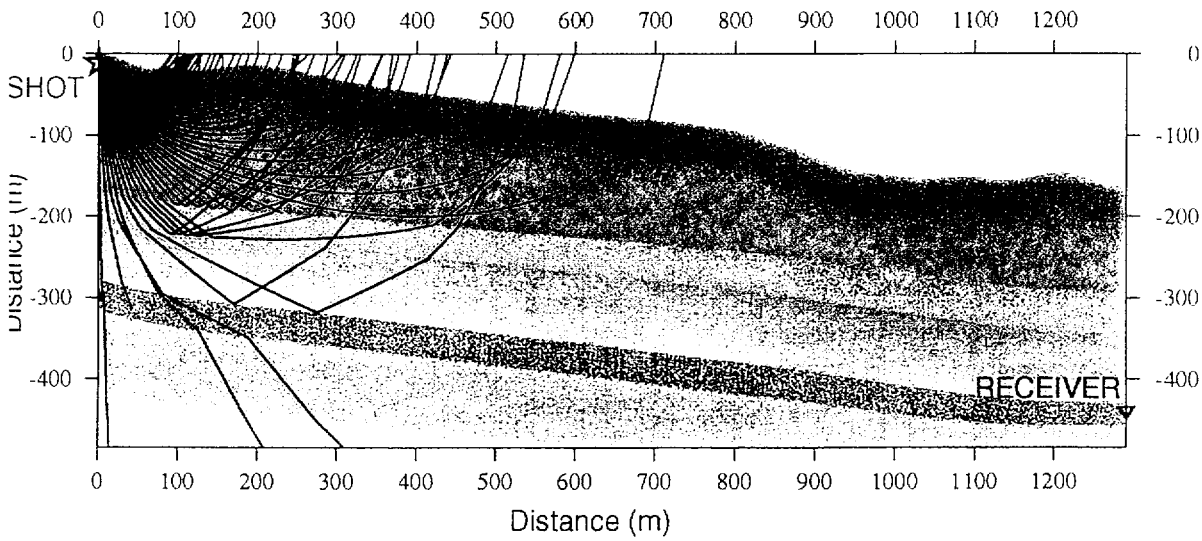

Figure 12. Crossection through final velocity model with the source (star) in the upper left corner and the receiver (triangle) inside the tunnel in the middle-nonlithophysal zone (orange). Black lines show the seismic ray paths. The rays were shot using take-off angle between 40 degrees and 90 degrees. Geology from Clayton, 1998.

NOT APPROVED

DO NOT COPY OR DUPLICATE

PRELIMINARY DRAFT

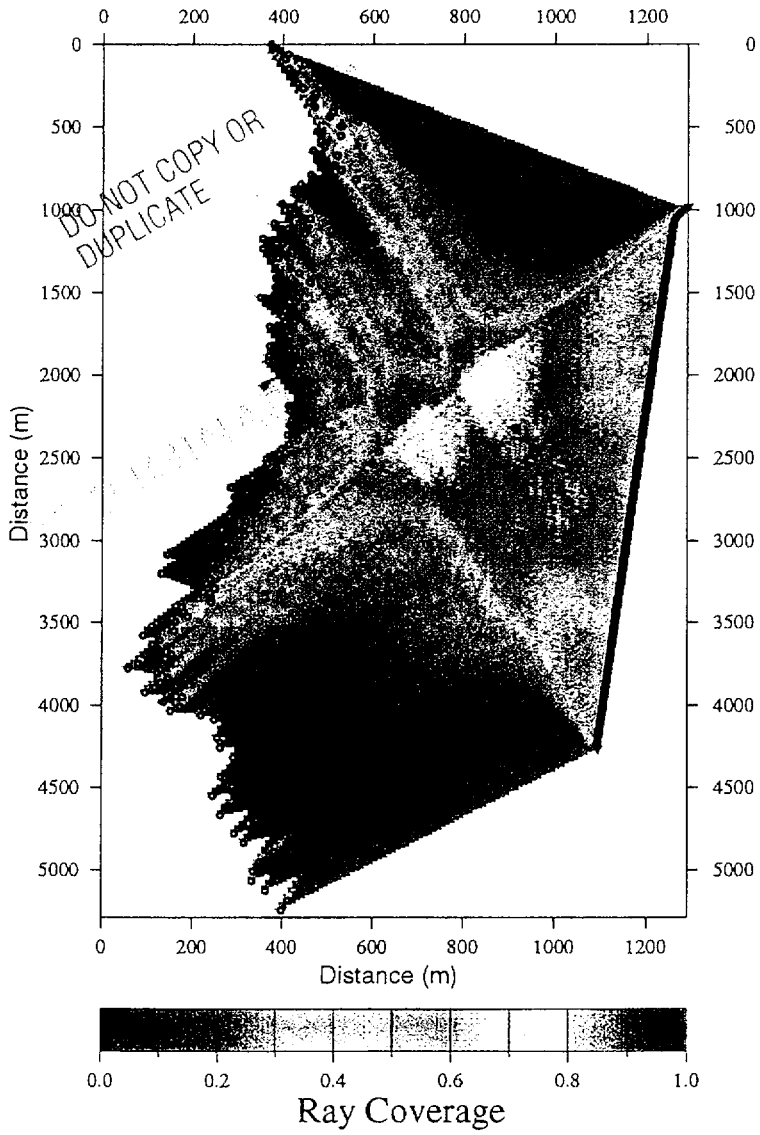

Figure 13. Density of seismic ray coverage in the imaged horizon (middle-nonlithophysal zone), with relocated sources (circles) and receivers (triangles). Note that the origin of the current coordinate system is at (170054.02, 235191.92) in Nevada state coordinates in meters. Shown in color is the ray coverage normalized by the maximum number of rays in any cell (the maximum was 551). Cells with less than 10% (55 rays) are not used in the interpretation. (DTN:LB980930123112.001)

NOT APPROVED

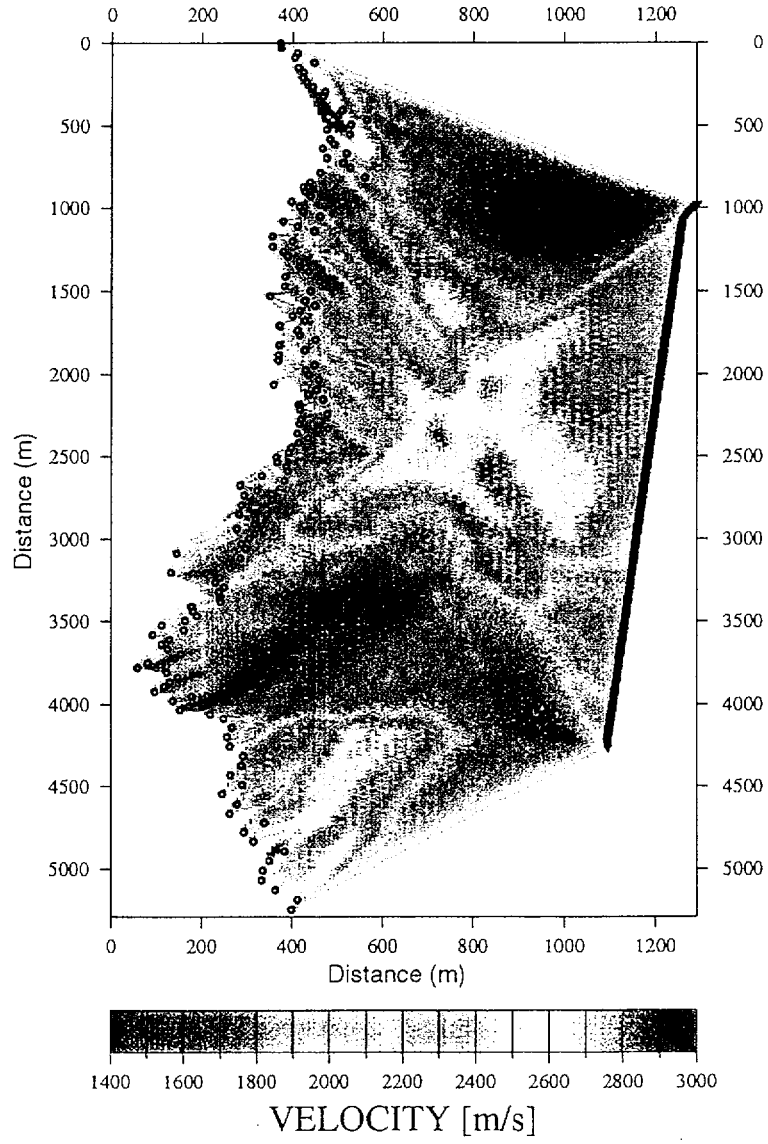

Figure 14. Shown are the P wave velocity estimates of the initial travel time inversion without source static correction. (DTN: LB980930123112.001)

DO NOT COPY OR DUPLICATE

DO NOT COPY OR DUPLICATE

NOT APPROVED

PRELIMINARY DRAFT

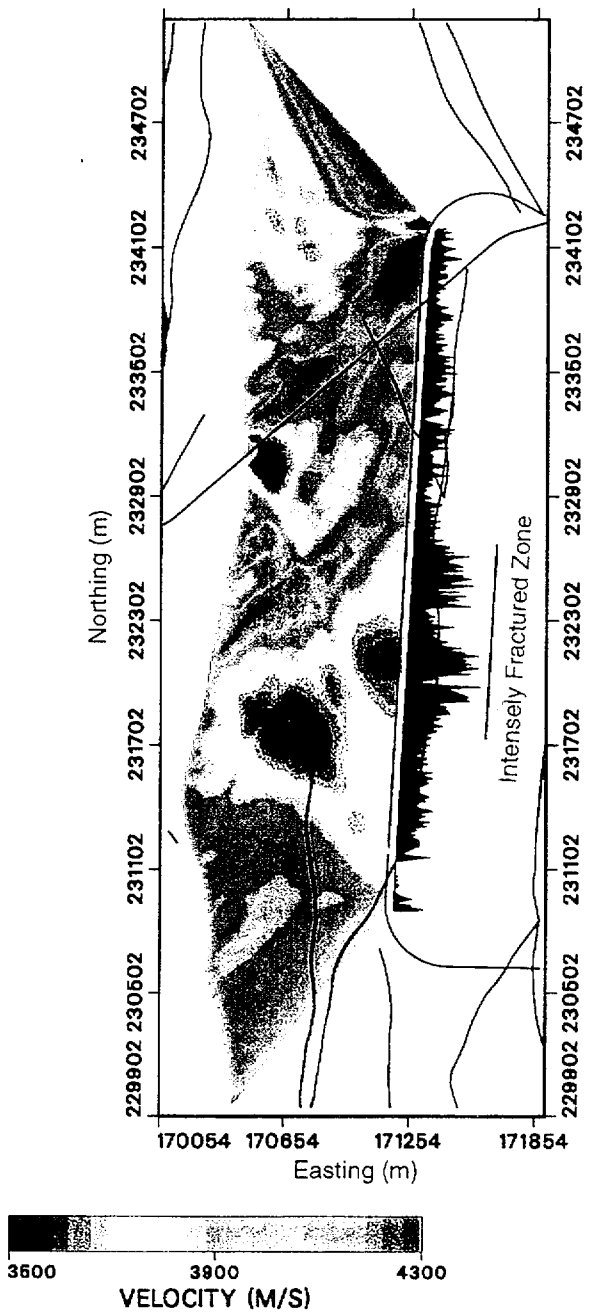

Figure 15 The final travel time inversion using source static corrections. The ESF and crossdrift tunnels and major faults are drawn as black lines. The coordinates are Nevada state plane in meters. (DTN:LB980930123112.001)

DO NOT COPY OR DUPLICATE

NOT APPROVED

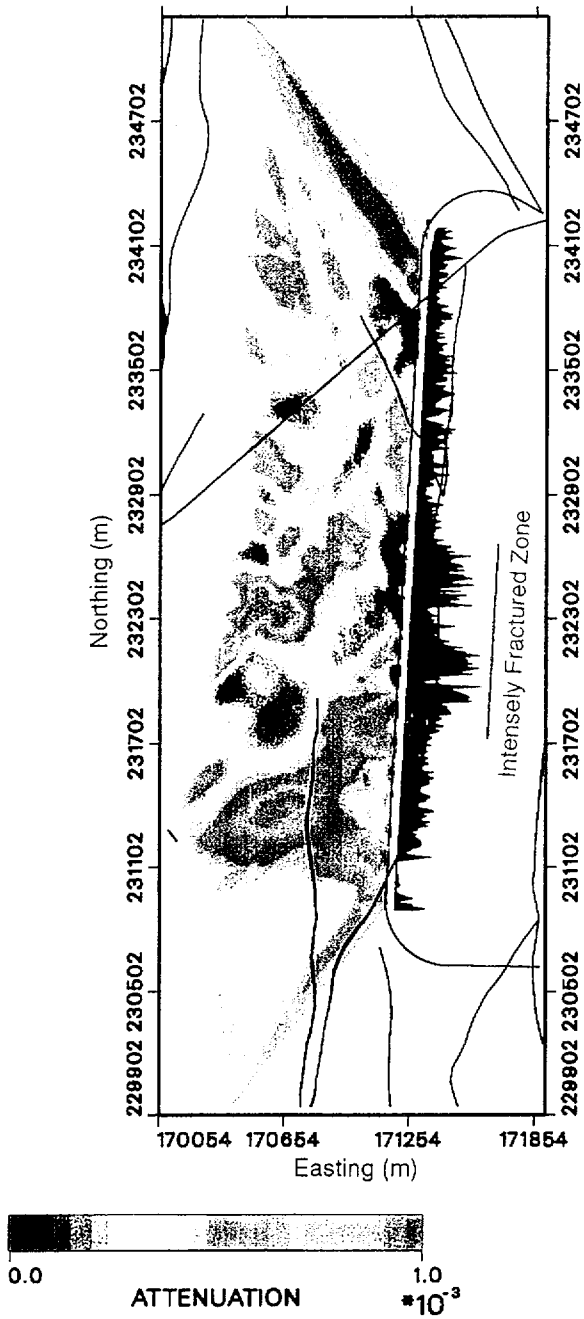

PRELIMINARY DRAFT

Figure 16 Amplitude attenuation tomogram using source static corrections. The ESF and crossdrift tunnels and major faults are drawn as black lines. The coordinates are Nevada state plane in meters. (DTN:LB980930123112.001)

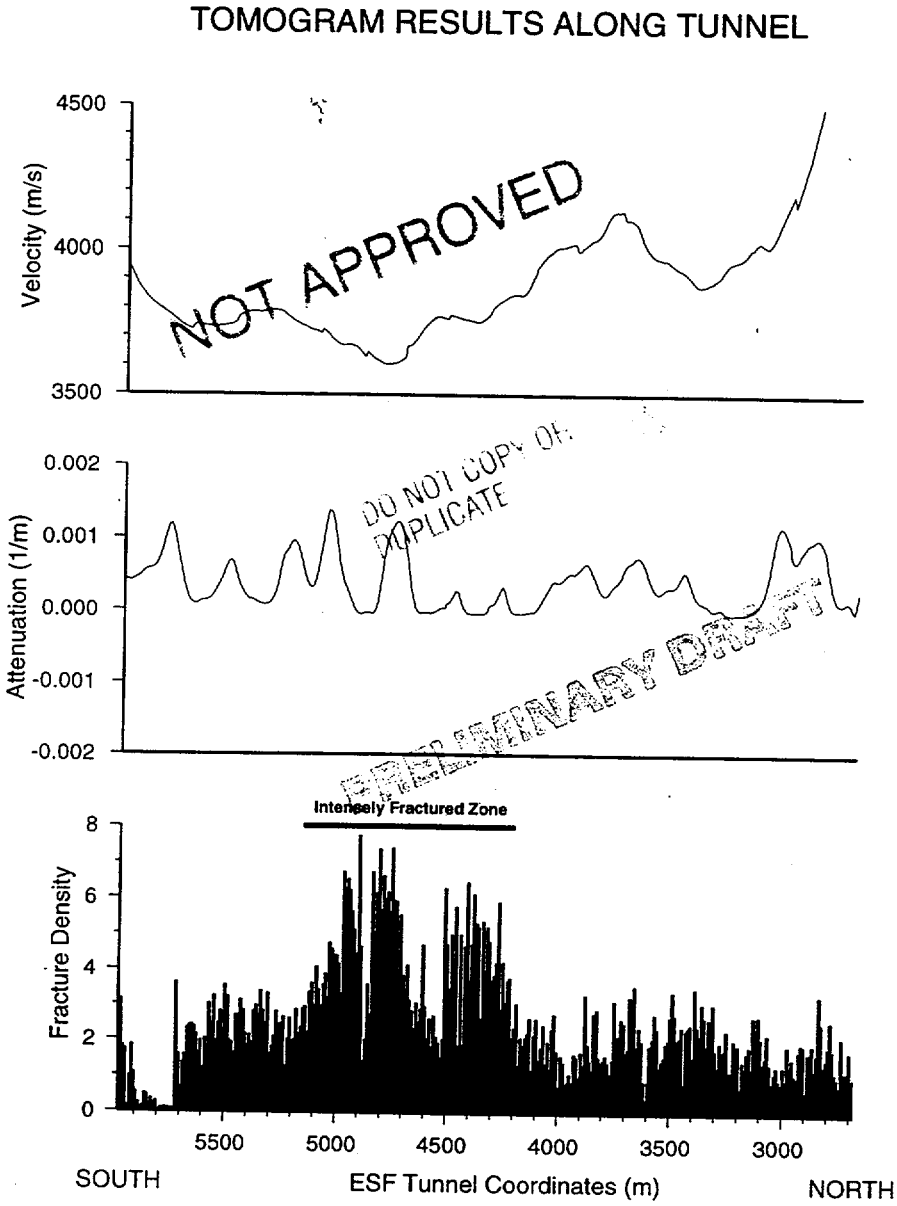

Figure 17 Comparison of velocity (top) and attenuation (middle) tomogram values at the ESF tunnel with fracture density mapped in the ESF tunnel (bottom). Note that a broad velocity low corresponds with increased fracturing and that minimums of attenuation correspond with peaks of fracture density, (USGS, Beason). (DTN:LB980930123112.001)

DO NOT COPY OR DUPLICATE

NOT APPROVED

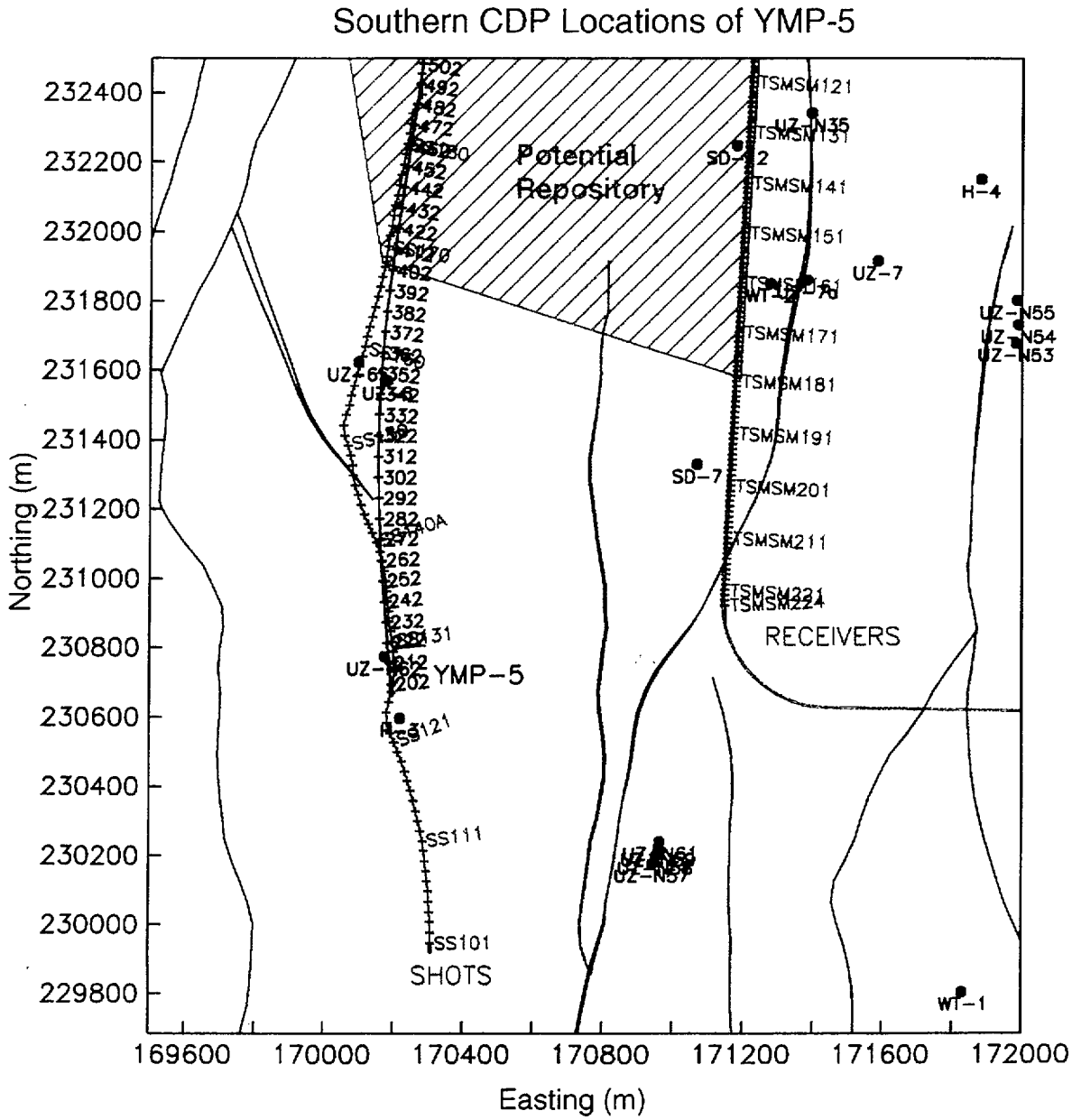

Figure 18 Area of interest for the reprocessing of surface seismic reflection profile YMP-5. The location of YMP-5 CDPs are shown in black from 202 to 502. The tomography source locations are SS101 to SS180; the tomography receivers are in blue as TSMSM121 to TSMSM224. The ESF tunnel is in orange and major faults are in red and nearby wells are in black. The current proposed repository location is in green. (DTN:LB980930123112.001) and Geology from Clayton, 1998.

PRELIMINARY DRAFT

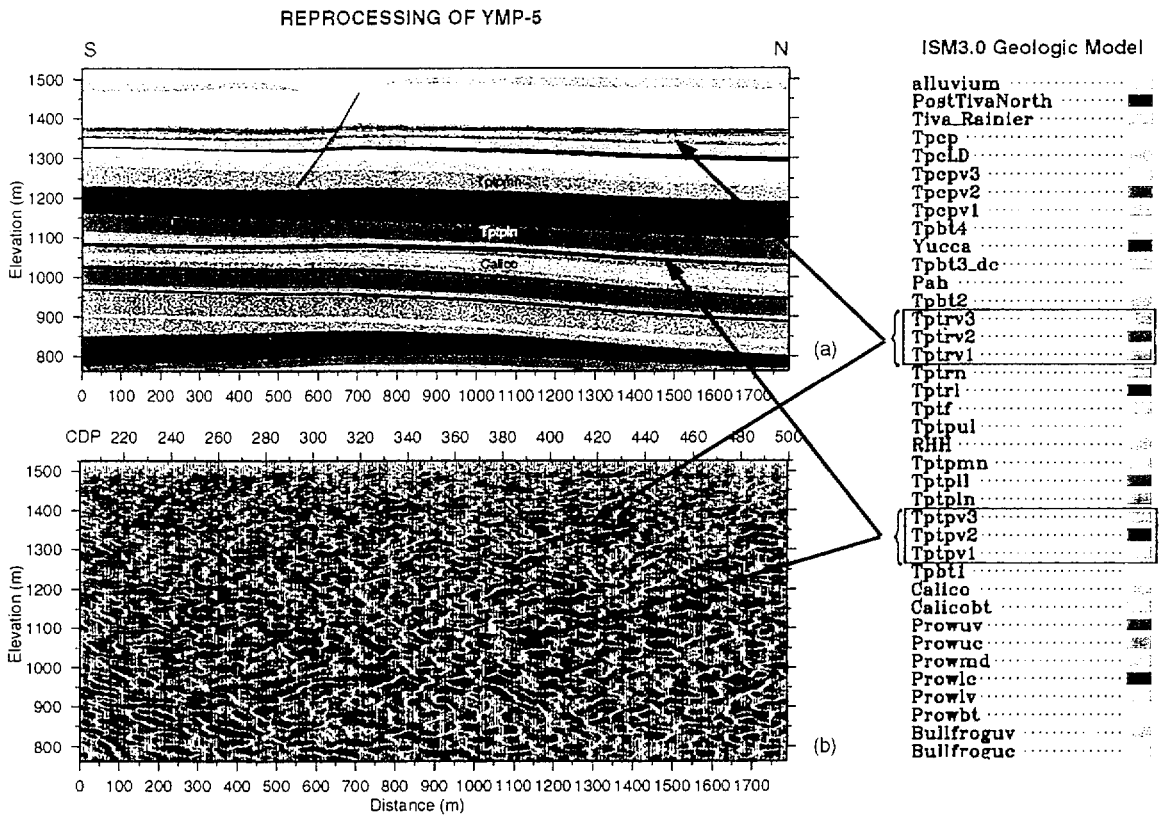

Figure 19 Results from reprocessing of line YMP-5 (bottom) along with the current geologic cross section (top). Our current interpretation of the reflectors associated with Tptrv and Tptpv are shown in yellow highlight on YMP-5 (bottom).

NOT APPROVED
DO NOT COPY OR DUPLICATE
PRELIMINARY DRAFT

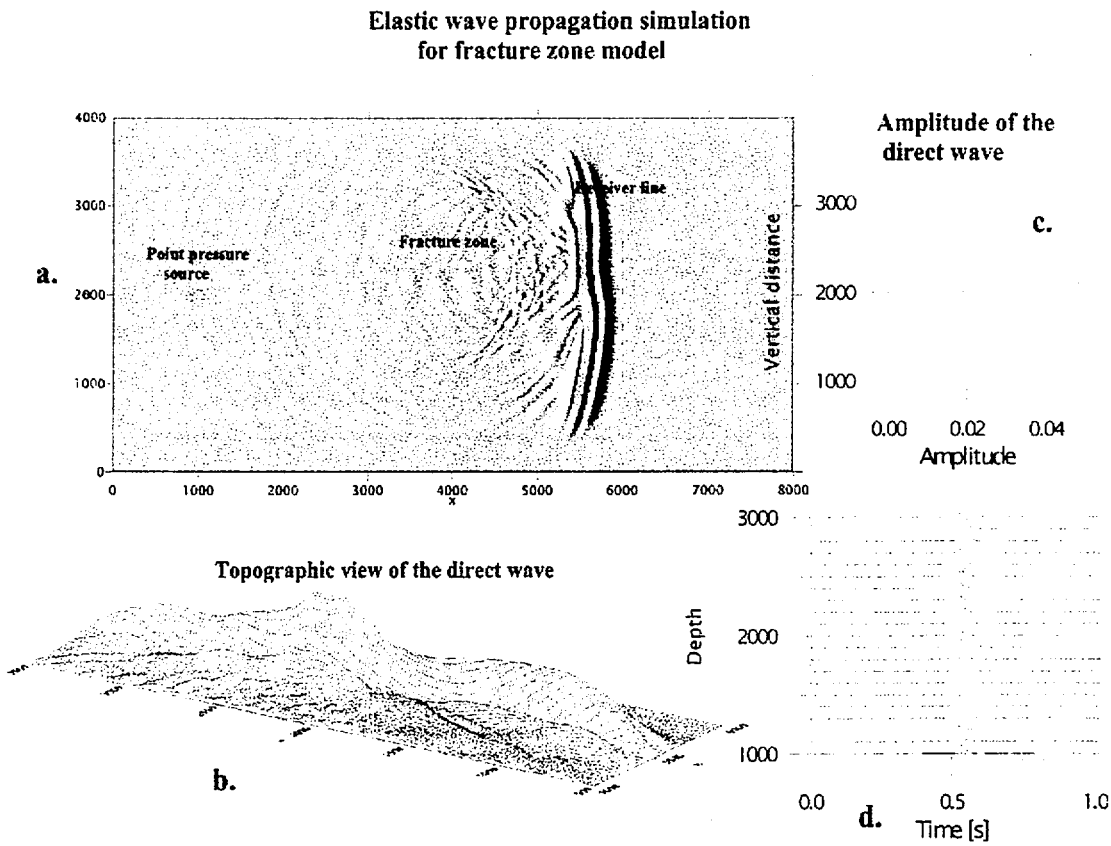

Figure 20 Results of modeling elastic wave propagation through a set of fractures with fm2d, shown are the model in a., the arrival time along the zone in b., the amplitude values along the zone in c. and the individual waveforms in d.

NOT APPROVED

DO NOT COPY OR DUPLICATE

PRELIMINARY DRAFT

DO NOT COPY OR
DUPLICATE

NOT APPROVED

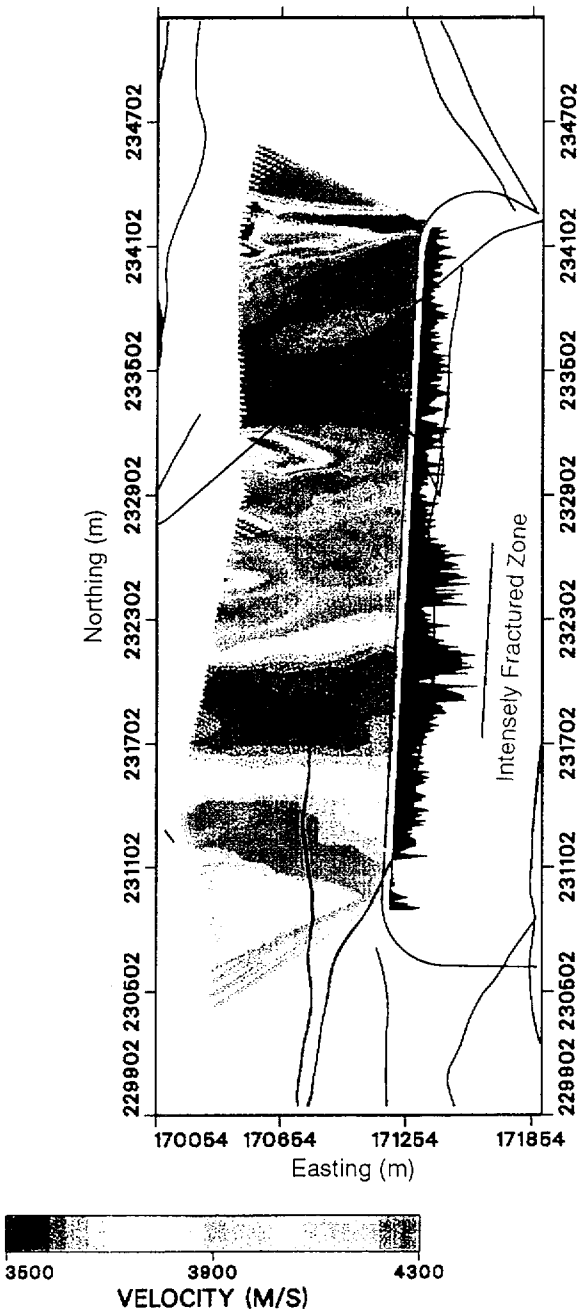

PRELIMINARY DRAFT

Figure 21a Velocity tomogram with only the rays of 30 degrees and less included. DTN:LB980930123112.001 and Clayton, 1998.

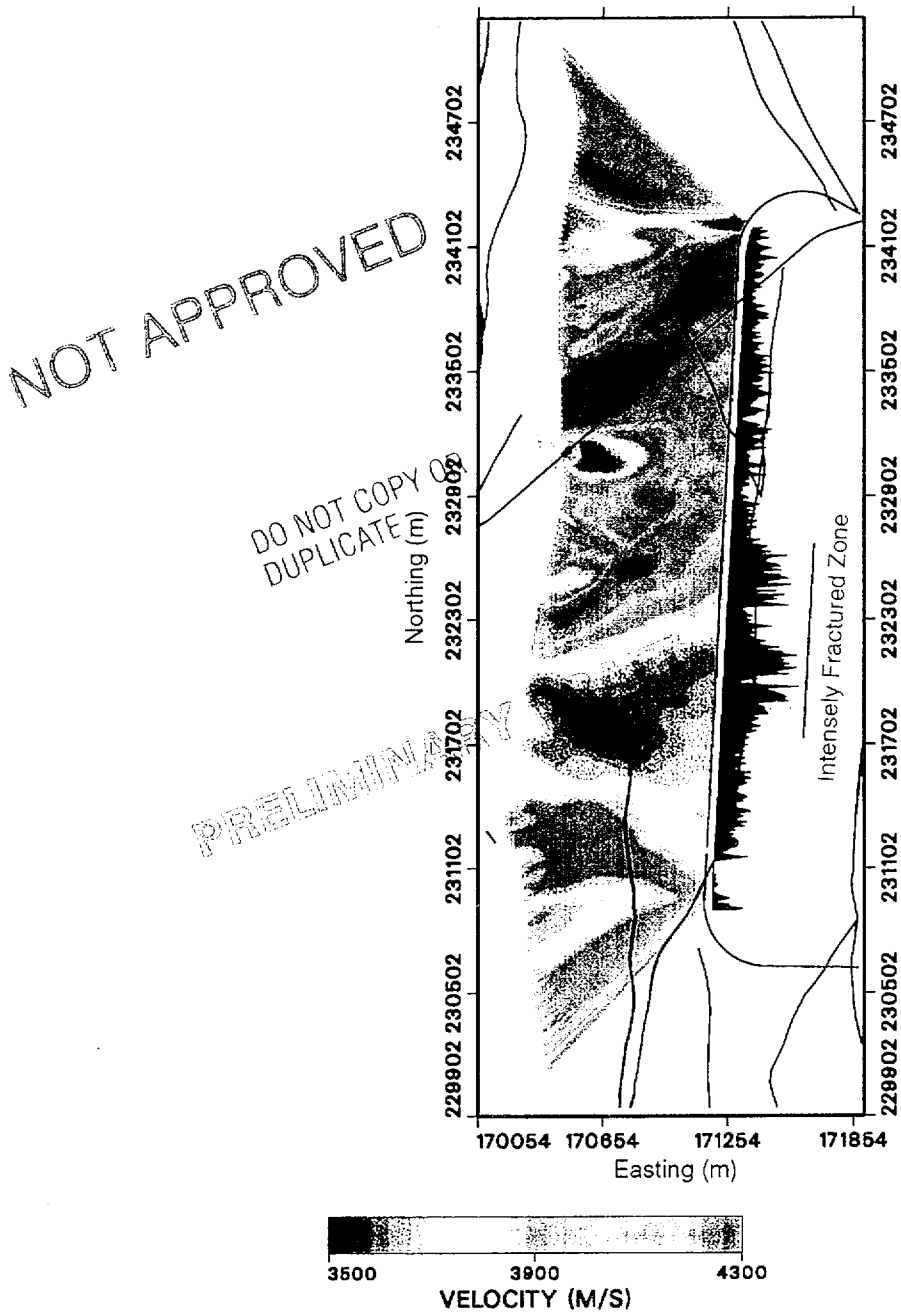

Figure 21b Velocity tomogram with only the rays of 45 degrees and less included. DTN:LB980930123112.001 and Clayton, 1998.

DO NOT COPY OR DUPLICATE

PRELIMINARY DRAFT

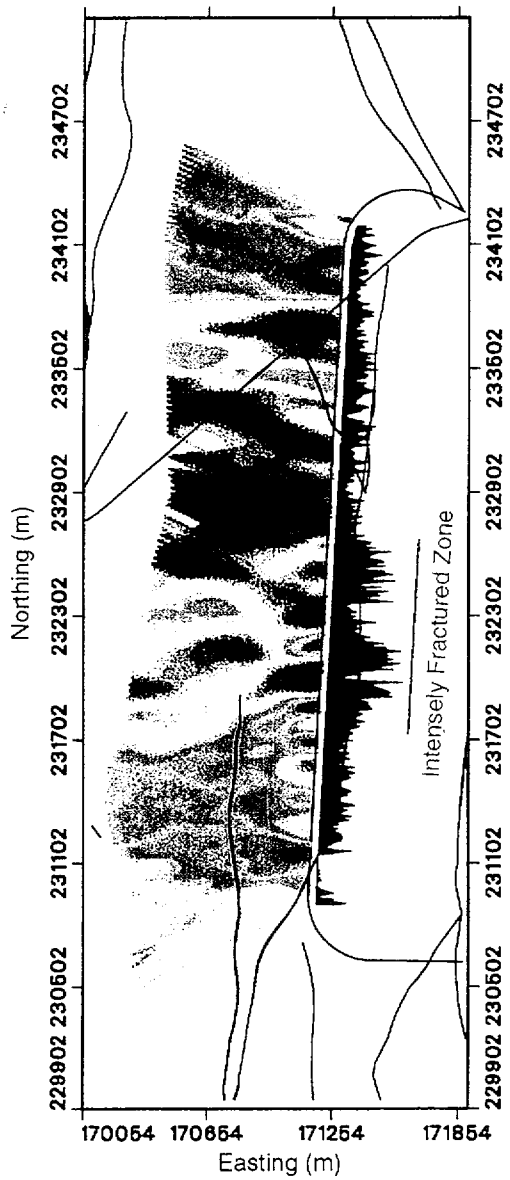

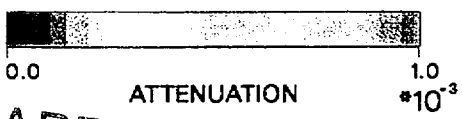

NOT APPROVED

Figure 21c Amplitude tomogram with only the rays of 30 degrees and less included. DTN:LB980930123112.001 and Clayton, 1998.

NOT APPROVED

DO NOT COPY OR DUPLICATE

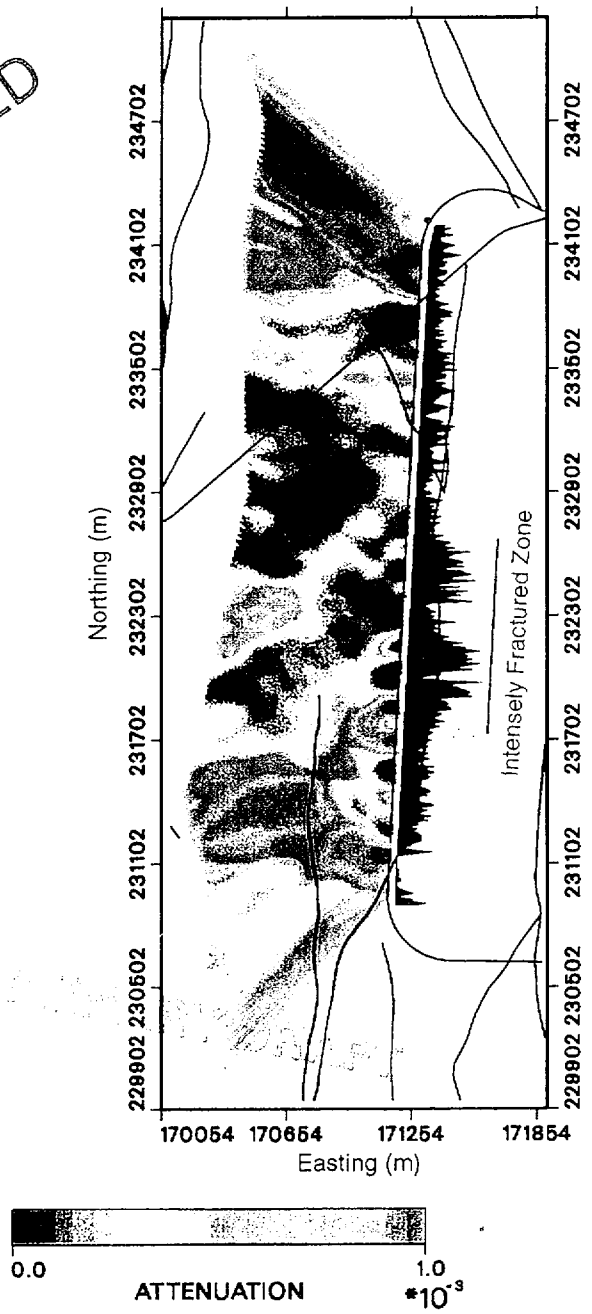

Figure 21d Amplitude tomogram with only the rays of 45 degrees and less included. DTN:LB980930123112.001 and Clayton.

DO NOT COPY OR DUPLICATE

NOT APPROVED

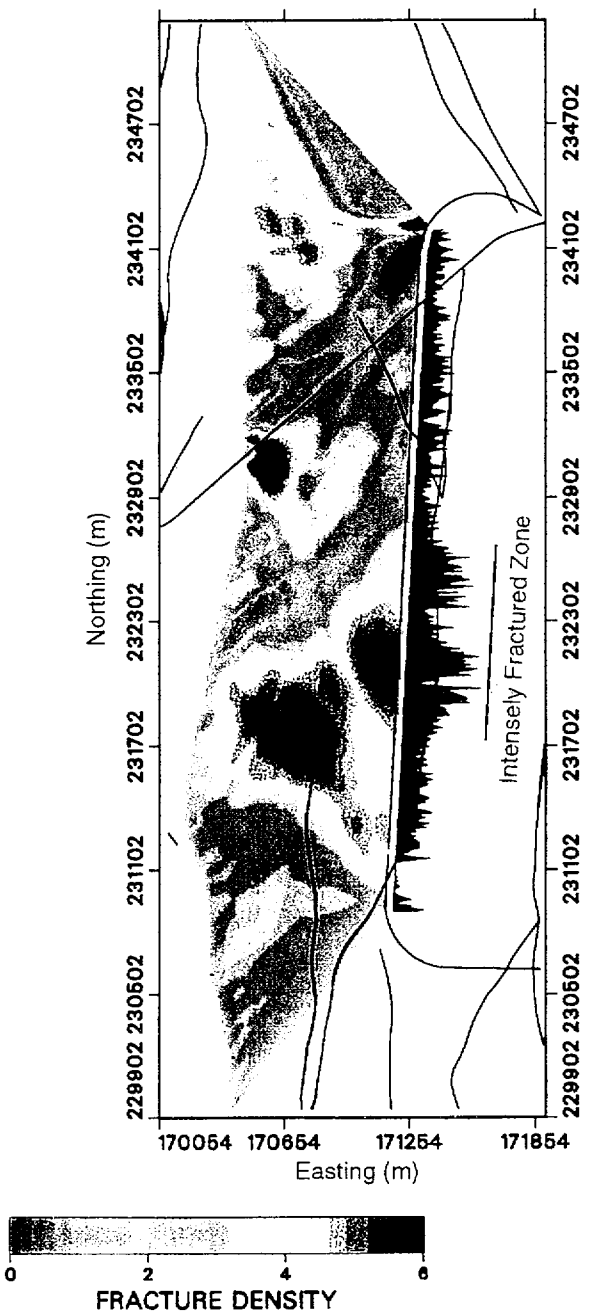

PRELIMINARY DRAFT

Figure 22 A tomogram of the fracture density. It has not been normalized to the actual fracture density mapped in the ESF, but it is a broad characterization of the variability of fracture density in the zone mapped. Fracture density is shown in fractures per cubic meter. DTN:LB980930123112.001 and Clayton.

NOT APPROVED

DO NOT COPY OR DUPLICATE

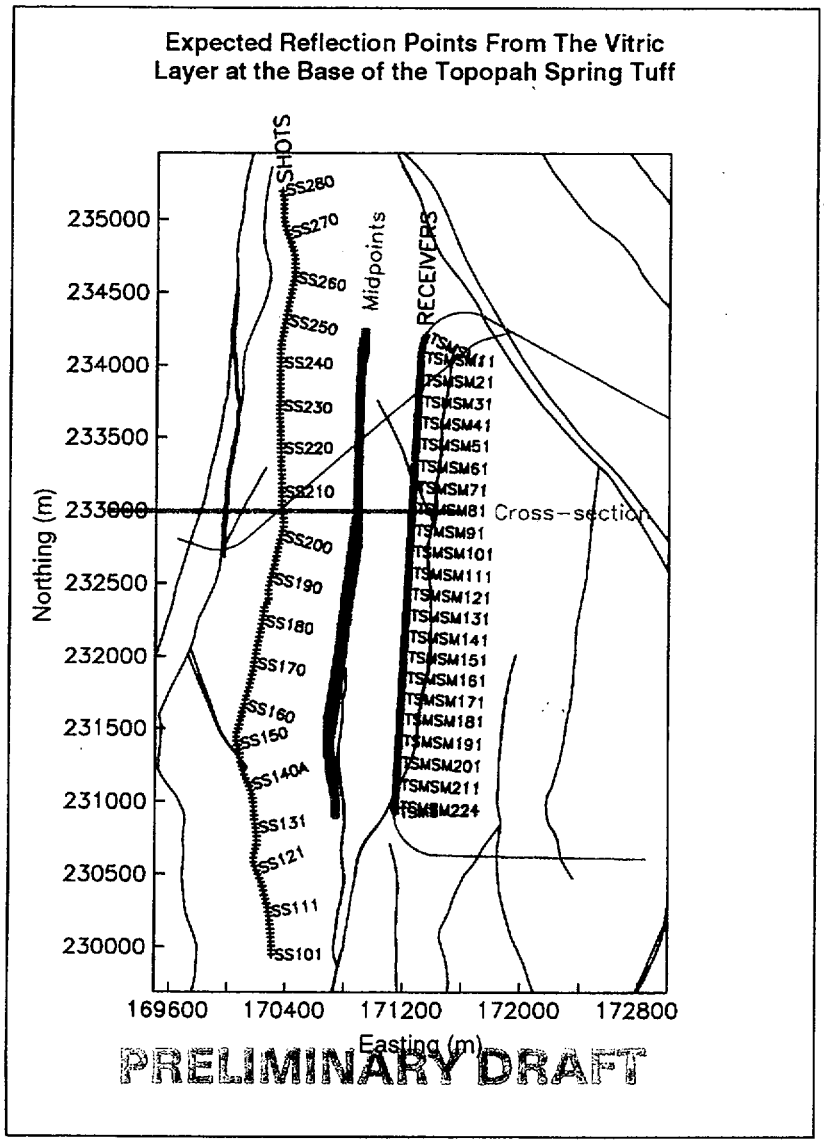

Figure 23 Ray traced modeling results for a CMP (common mid-point)stack of the surface to tunnel tomography data at the Tptprv horizon. The green band of points oriented north-south in the center of the figure is the CMP points. This modeling indicates that reflection processing would give a high fold, essentially 2D reflection image of the Tptprv. DTN:LB980930123112.001 and Clayton (1998).

NOT APPROVED

DO NOT COPY OR DUPLICATE

Numerical modeling of tunnel to tunnel zero offset seismic experiment

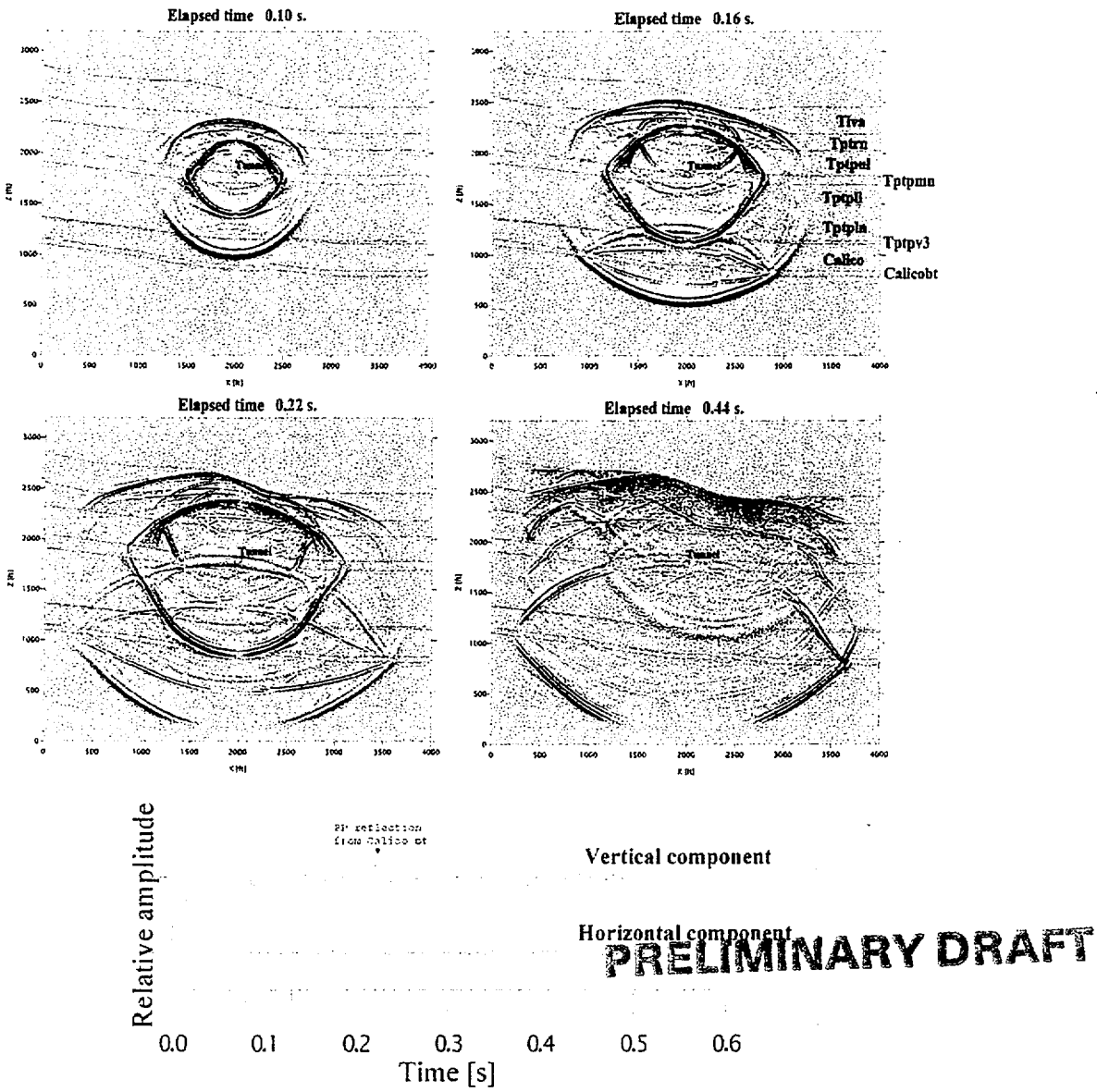

PRELIMINARY DRAFT

Figure 24 2D modeling results from tunnel to tunnel geometry. Time snapshots show wavefronts propagating through the medium with reflections and mode conversions both above and below the tunnel. Synthetic seismograms (bottom) for a vertical and a horizontal receiver show the relative strength of the reflections from the base of the Calico Hills Formation.